OSTQUANT: REFINING LARGE LANGUAGE MODEL QUANTIZATION WITH ORTHOGONAL AND SCALING TRANSFORMATIONS FOR BETTER DISTRIBUTION FITTING

Anonymous authors
Paper under double-blind review

ABSTRACT

Post-training quantization (PTQ) has emerged as a widely adopted technique for compressing and accelerating Large Language Models (LLMs). The major challenge in LLM quantization is that uneven and heavy-tailed data distributions can expand the quantization range, thereby reducing bit precision for most values. Recent methods attempt to eliminate outliers and balance inter-channel differences by employing linear transformations; however, they remain heuristic and are often overlook optimizing the data distribution across the entire quantization space. In this paper, we introduce Quantization Space Utilization Rate (QSUR), a novel metric that effectively assesses the quantizability of transformed data by measuring the space utilization of the data in the quantization space. We complement QSUR with mathematical derivations that examine the effects and limitations of various transformations, guiding our development of Orthogonal and Scaling Transformation-based Quantization (OSTQuant). OSTQuant employs a learnable equivalent transformation, consisting of an orthogonal transformation and a scaling transformation, to optimize the distributions of weights and activations across the entire quantization space. Futhermore, we propose the KL-Top loss function, designed to mitigate noise during optimization while retaining richer semantic information within the limited calibration data imposed by PTQ. OSTQuant outperforms existing work on various LLMs and benchmarks. In the W4-only setting, it retains 99.5% of the floating-point accuracy. In the more challenging W4A4KV4 configuration, OSTQuant reduces the performance gap by 32% on the LLaMA-3-8B model compared to state-of-the-art methods. Code will be available.

1 INTRODUCTION

Large language models (LLMs) (Dettmers et al., 2022; Touvron et al., 2023a;b) have demonstrated exceptional performance across a variety of tasks, increasingly integrating into daily life and playing critical roles in various areas (Achiam et al., 2023; Chen et al., 2024). Nevertheless, the substantial memory and computational demands pose significant deployment challenges, limiting their practical applicability not only on edge devices with constrained resources but also on cloud servers equipped with powerful GPU devices.

Post-training quantization (PTQ) has emerged as a widely adopted technique for compressing and accelerating LLMs. During quantization, uneven and heteroscedastic data, as shown in 1(a), pose significant challenges, as they expand the quantization range and reduce available bit precision for the majority of values. Recently researches (Xiao et al., 2022; Shao et al., 2023; Ma et al., 2024; Ashkboos et al., 2024) have employed linear transformations to tackle these challenges, showing effectiveness in improving data distribution in specific regions of the quantization space. For instance, smooth-based transformations like SmoothQuant (Xiao et al., 2022) alleviate activation quantization difficulty by redistributing it to weights, reducing inter-channel variance. Similarly, rotation-based methods such as Quarot use rotation techniques to suppress outliers. However, these approaches remain heuristic and do not optimize the distribution across the entire quantization space.

In this paper, we introduce the concept of Quantization Space Utilization Rate (QSUR) as a more effective metric for evaluating the quantizability of transformed data. We define QSUR as the ratio of

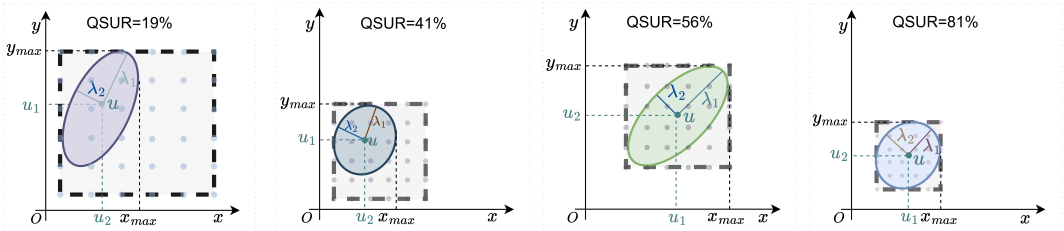

(a) Original (b) Smooth Transform (c) Rotation Transform (d) Ours

Figure 1: Transformation of a batch of two-dimensional data $X \sim \mathcal{N}(\boldsymbol{\mu}, \boldsymbol{\Sigma})$ using different methods. Eigenvalues λ_1 and λ_2 represent the spread of the distribution along principal axes after eigenvalue decomposition of Σ . (a) shows the original distribution, while (b), (c), and (d) illustrate the effects of the Smooth-based, Rotate-base, and ours OST-based methods, respectively, on QSUR. The ellipse represents the space occupied by the data, and the square indicates the quantization space required to quantize this distribution, determined by the maximum and minimum values of it. The gray dots within the square denote the specific quantization points within the quantization space. The higher the number of quantization points within the ellipse, the greater the quantization space utilization rate of the distribution.

the volume occupied by a set of data X to the volume of the quantization space corresponding to X. Given that weights and activations typically exist in multiple dimensions, this quantization space is modeled as a hypercube where the edge lengths are determined by the maximum quantization range across all dimensions of the data. Experiments demonstrate a positive correlation between QSUR and quantization accuracy (as shown in Fig 3), suggesting that higher QSUR values contribute to improved quantization precision. In addition, we complement QSUR with mathematical derivations (refer to Sec 3 for more details), which examine the effects and limitations of linear transformations and establishes a theoretical foundation for developing more effective transformation. As shown in Fig 1, as QSUR increases, the data distribution becomes flatter, allowing more quantization levels to be utilized. Smooth-based and rotation-based transformations improve QSUR from different perspectives: smooth-based transformations excel at reducing variations among eigenvalues, whereas rotation-based transformations adeptly balance feature orientations and harmonize mean values across dimensions. However, these approaches encounter a critical limitation: their effectiveness is restricted to specific regions within the quantization space, leading to low utilization rates.

To this end, we propose Orthogonal and Scaling Transformation-based Quantization (OSTQuant). OSTQuant assigns a learnable equivalent transformation pair—comprising an orthogonal transformation and a scaling transformation—to each fully connected (FC) layer in LLMs. During optimization, these transformation pairs aim to optimize the distributions of weights and activations across the entire quantization space. The transformation pairs and their inverses are then fused into their respective FC layers, preserving the original computational graph. Besides, unlike block-wise reconstruction methods (Shao et al., 2023; Ma et al., 2024), our equivalent transformation pairs do not alter network's final output, ensuring generalization and avoiding overfitting to the calibration set.

Another challenge is that, unlike the original floating-point models trained on large datasets, PTQ is typically conducted on a small calibration set (e.g., 1000 or fewer). In this context, persisting with the original cross-entropy loss may result in a decline in model performance. To mitigate this problem, we introduce KL-Top loss function, which leverages the top k highest-probability logits from the full-precision model, rather than concentrating solely on the logit probability corresponding to the correct label. Our KL-Top loss improves the capture of more nuanced semantic information while mitigating noise from the long-tail distribution in the full KL divergence. As for optimizer, we employ RiemannAdam (James, 1976), a proficient technique tailored for learning Stiefel Manifolds using first-order information.

OSTQuant is an effective and efficient PTQ method for LLMs, outperforming existing approaches across various models and benchmarks. In the W4-only setting, it retains above 99.5% of the floating-point accuracy. In the more challenging W4A4KV4 configuration, OSTQuant reduces the performance gap by 32% on LLaMA-3-8B compared to state-of-the-art (SOTA) methods. In terms of speed, it can complete the quantization of LLaMA-3-8B on an A800 GPU in just 20 minutes. Our contributions are summarized as follows:

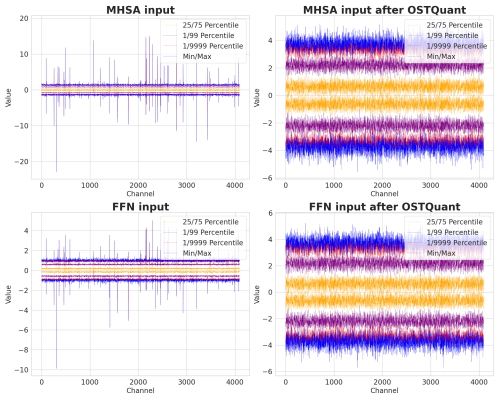

Figure 2: Activation distribution in the LLaMA-3-8B before and after applying OSTQuant shows significant differences. Prior to transformation, the distribution across different channels exhibits substantial variation and contains numerous outliers. After OSTQuant, the distributions become more uniform across channels.

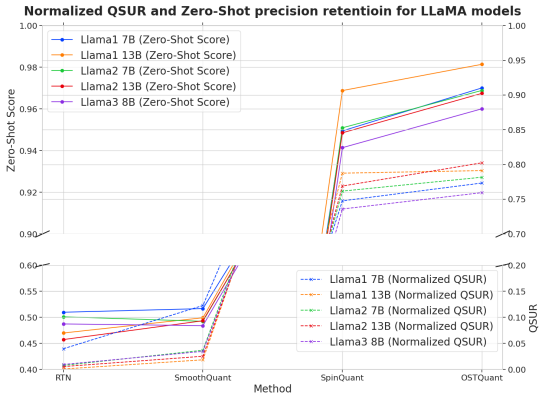

Figure 3: Zero-Shot[9] precision retention (under W4A4 quantization) and normalized QSUR are evaluated for LLaMA variants across different quantization methods. The normalized QSUR is derived as the d-th root of QSUR, where d denotes the number of channels. QSUR exhibits a positive correlation with accuracy.

- We introduce the concept of Quantization Space Utilization Rate (QSUR) as an effective metric to evaluate quantizability. We also complement QSUR with mathematical derivations that examine the effects and limitations of various transformations, guiding the next steps in optimization and method design.
- We propose OSTQuant, a fast and effective PTQ method. It improves QSUR and quantization performance by globally optimizing multiple equivalent transformation pairs in LLMs, each consisting of a scaling transformation and an orthogonal transformation. To address the challenge of limited datasets imposed by PTQ during optimization, we introduce the KL-Top loss, which captures richer semantic information from the model while mitigating the impact of label noise.
- Building on these advancements, our method demonstrates robust performance in both weight-only, weight-activation and weight-activation-kvcache quantization modes. In the W4A16 configuration, it retains over 99.5% of the full precision accuracy, while in the more aggressive W4A4KV4 setting, it maintains at least 96% of the model's original performance.

2 Related Work

Post Training Quantization(PTQ) for LLMs. Post-training quantization (PTQ) has become a mainstream technique for LLMs due to its efficiency. Existing PTQ methods can be broadly divided into weight-only and weight-activation quantization. To reduce memory usage, some approaches focus on weight-only quantization. GPTQ (Frantar et al., 2022) uses Hessian-based error compensation to achieve high compression rates by minimizing quantization errors. AWQ (Lin et al., 2023) and OWQ (Lee et al., 2023) improve performance by addressing the impact of activation outliers on weight quantization. QuIP (Chee et al., 2023) and QuIP# (Tseng et al., 2024) use random Hadamard matrices for incoherent processing and apply vector quantization to weights, achieving better performance with reduced precision quantization. Unlike weight-only methods, weight-activation quantization aims to speed up LLM inference by quantizing both weights and activations, including the key-value (KV) cache. The main challenge in activation quantization is that outliers dominate the range, leaving few significant bits for most values, leading to substantial errors. ZeroQuant (Yao et al., 2022) proposes a fine-grained hardware-friendly quantization scheme for both weights and activations. SmoothQuant (Xiao et al., 2022) shifts quantization difficulty from activations to weights through mathematical transformation. OmniQuant (Shao et al., 2023) further enhances performance by training quantization parameters and transformation coefficients. Moreover, I-LLM (Hu et al., 2024) achieves integer-only quantization and inference through fully-smooth block reconstruction and fully integer operators. Recently, QuaRot (Ashkboos et al., 2024) uses random rotation matrices to enable

4-bit quantization of weights and activations, while SpinQuant (Liu et al., 2024) learns these matrices to refine 4-bit quantization.

Riemannian Optimization. The optimization of rotation matrices necessitates adherence to orthonormality constraints, which corresponds to performing Riemannian optimization on the Stiefel manifold (James, 1976), encompassing all orthogonal matrices. Cayley SGD (Li et al., 2020) relies on iterative approximations of the Cayley Transform, achieved solely by matrix multiplication, enabling effective optimization of rotation matrices for arbitrary loss functions. RAOM (Bécigneul & Ganea, 2018) extends optimization methods such as ADAM (Kingma, 2014), ADAGRAD, and AMSGRAD into the realm of Riemannian optimization. Meanwhile, Geoopt (Kochurov et al., 2020) supports fundamental Riemannian stochastic gradient descent (SGD) and adaptive optimization algorithms, facilitating seamless integration into models for comprehensive optimization.

3 Quantization Space Utilization Rate

Although significant progress has been made PTQ using linear transformations to mitigate quantization loss (Xiao et al., 2022; Ma et al., 2024; Ashkboos et al., 2024), these methods are primarily heuristic and result-driven, lacking a quantitative metric to assess quantization difficulty or the effectiveness of different transformations. To address this gap, we introduce a novel metric, the Quantization Space Utilization Rate (QSUR), which quantifies how effectively weight or activation distributions utilize the available quantization space. QSUR provides critical insights into the strengths and limitations of existing methods and lays the groundwork for developing more efficient approaches, including our OSTQuant method described in Sec 4.1.

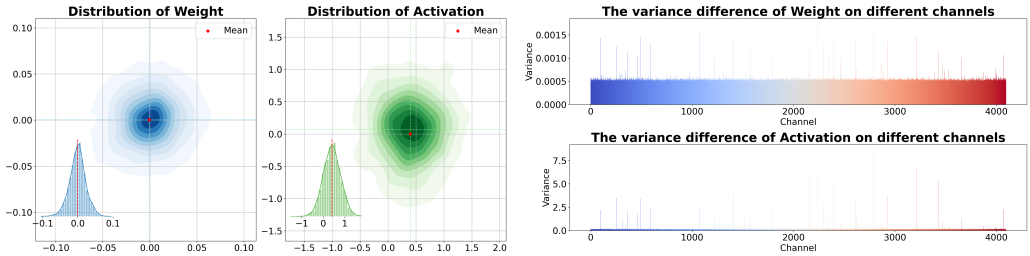

(a) (b)

Figure 4: The distribution of activation and weight in LLaMA-2 7B. (a) The weight and activation distributions exhibit a Gaussian pattern. The red dots indicate the mean value of the distributions. Both the weights and activations are projected onto a two-dimensional space. (b) The inter-channel variance disparities between weights and activations. In comparison with weights, the inter-channel disparities of activations are more pronounced.

Quantization Notations. In this section, we define the key notations used in quantization. Matrices are denoted by bold uppercase letters (e.g., $\boldsymbol{X}$), while vectors are denoted by bold lowercase letters (e.g., $\boldsymbol{x}$). The operator $\mathcal{Q}$ refers to the quantization function. For a comprehensive list of mathematical symbols and definitions, please refer to Appendix A.1, where additional details on quantization and dequantization are also provided.

Lemma 1. *By the central limit theorem, the distribution after Hadamard transformation follows an approximately ball-shaped Gaussian distribution, as demonstrated in QuIP# (Tseng et al., 2024).*

Definition 1. Given a set of d-dimensional data $\boldsymbol{X} \in \mathbb{R}^{n\times d}$, let $V_{\boldsymbol{X}}$ denote the hypervolume occupied by $\boldsymbol{X}$, and $V_{S_{\boldsymbol{X}}}$ denote the hypervolume of the quantization space S corresponding to X. The quantization space $S_{\boldsymbol{X}}$ is a hypercube whose edge lengths are defined by the maximum quantization range across all dimensions of $\boldsymbol{X}$. **The Quantization Space Utilization Rate** of $\boldsymbol{X}$ is then defined as:

$$\text{QSUR}_{\boldsymbol{X}} = \frac{V_{\boldsymbol{X}}}{V_{S_{\boldsymbol{X}}}} \tag{1}$$

Given $X \sim \mathcal{N}(\boldsymbol{\mu}, \boldsymbol{\Sigma})$. $V_{\boldsymbol{X}}$ is calculated based on the ellipsoid formed by the covariance matrix $\boldsymbol{\Sigma}$ and mean vector $\boldsymbol{\mu}$. The covariance matrix can be diagonalized via eigenvalue decomposition: $\boldsymbol{\Sigma} = \boldsymbol{Q}\boldsymbol{\Lambda}\boldsymbol{Q}^\top$, where $\boldsymbol{Q}$ is a unit orthogonal matrix of eigenvectors, and $\boldsymbol{\Lambda} = \text{diag}(\lambda_1, \lambda_2, \ldots, \lambda_d)$ contains the eigenvalues in descending order. The hypervolume of this ellipsoid at confidence level α (e.g., $\alpha = 0.99$) is given by:

$$V_{\boldsymbol{X}} = \frac{\pi^{d/2}}{\Gamma(d/2+1)} \times \left(\chi_d^2(\alpha)\right)^{d/2} \times \sqrt{\det(\boldsymbol{\Sigma})} \tag{2}$$

where Γ is the Gamma function and $\chi_d^2(\alpha)$ is the chi-squared quantile. Since $\boldsymbol{Q}$ is orthogonal, the determinant simplifies to $\det(\boldsymbol{\Sigma}) = \det(\boldsymbol{\Lambda})$. The volume of the quantization hypercube, V_{S_X}, is determined by the range of the distribution along each principal axis. The extremal points of the ellipsoid are closely correspond to the maximum and minimum along these axes. We denote the eigenvalues of the principal axes corresponding to the points with the maximum and minimum coordinate values as $\lambda_{\max}$ and $\lambda_{\min}$, respectively. After transforming these points back to the original space, the maximum and minimum coordinate values can be represented as:

$$\boldsymbol{v}_{\max}^{\text{org}} = \sqrt{\chi_d^2(\alpha) \cdot \lambda_{\max}} \cdot \boldsymbol{q}_{\max} + \boldsymbol{\mu} \tag{3}$$

$$\boldsymbol{v}_{min}^{\text{org}} = -\sqrt{\chi_d^2(\alpha) \cdot \lambda_{\min}} \cdot \boldsymbol{q}_{\min} + \boldsymbol{\mu} \tag{4}$$

$$V_{S_X} = (\max(\boldsymbol{v}_{\max}^{\text{org}}) - \min(\boldsymbol{v}_{\min}^{\text{org}}))^d \tag{5}$$

where $\boldsymbol{q}_{\max}$ and $\boldsymbol{q}_{\min}$ denote the eigenvectors corresponding to $\lambda_{\max}$ and $\lambda_{\min}$, respectively. Thus, the QSUR becomes:

$$\text{QSUR}_X = \frac{V_{\boldsymbol{X}}}{V_{S_{\boldsymbol{X}}}} = \frac{\frac{\pi^{d/2}}{\Gamma(d/2+1)} \cdot \left(\chi_d^2(\alpha)\right)^{d/2} \cdot \sqrt{\det(\boldsymbol{\Lambda})}}{\left(\max(\sqrt{\chi_d^2(\alpha) \cdot \lambda_{\max}} \cdot |\boldsymbol{q}_{\max}| + \boldsymbol{\mu}) - \min(\sqrt{\chi_d^2(\alpha) \cdot \lambda_{\min}} \cdot |\boldsymbol{q}_{\min}| + \boldsymbol{\mu})\right)^d} \tag{6}$$

Since the magnitude of the mean vector is often smaller than the largest eigenvalue. we neglect the mean vector $\boldsymbol{\mu}$, so $\lambda_{\max} = \lambda_{\min} = \lambda_1$, resulting in:

$$\text{QSUR}_{\boldsymbol{X}} = \frac{\frac{\pi^{d/2}}{\Gamma(d/2+1)} \cdot \left(\chi_d^2(\alpha)\right)^{d/2} \cdot \sqrt{\det(\Lambda)}}{2^d \left(\max(\sqrt{\chi_d^2(\alpha) \cdot \lambda_1} \cdot \boldsymbol{q}_1)\right)^d} = \frac{\frac{\pi^{d/2}}{\Gamma(d/2+1)} \cdot \sqrt{\prod_{i=1}^d \lambda_i}}{2^d \left(\max(\sqrt{\lambda_1} \cdot \boldsymbol{q}_1)\right)^d} \tag{7}$$

From Eq 7, we observe the following: 1) QSUR is proportional to the product of the ratios of each eigenvalue λ_i to the largest eigenvalue λ_1; 2) The maximum component of the eigenvector $\boldsymbol{q}_1$ is inversely proportional to QSUR. As demonstrated in Appendix A.2.1, when the components of $\boldsymbol{q_1}$ take values of $\pm d^{-1/2}$, the denominator in Eq 7 is minimized.

Influence of linear transformation on QSUR. Applying a linear transformation $\boldsymbol{T}$ to $\boldsymbol{X} \sim \mathcal{N}(\boldsymbol{\mu}, \boldsymbol{\Sigma})$ results in a transformed distribution $\hat{D} \sim \mathcal{N}(\hat{\boldsymbol{\mu}}, \hat{\boldsymbol{\Sigma}})$, where $\hat{\boldsymbol{\mu}} = \boldsymbol{T}\boldsymbol{\mu}$ and $\hat{\boldsymbol{\Sigma}} = \boldsymbol{T}\boldsymbol{Q}\boldsymbol{\Lambda}\boldsymbol{Q}^\top\boldsymbol{T}^\top$. Smoothing-based approaches (Xiao et al., 2022; Shao et al., 2023) treat $\boldsymbol{T}$ as a diagonal matrix that scales variances across different channel axes, indirectly reducing the disparities among the eigenvalues λ_i. However, these methods are particularly sensitive to outliers and uneven mean values, especially when the mean vector $\boldsymbol{\mu}$ contains significant variations like Fig 1(b). Moreover, when quantizing both weights and activations simultaneously, these methods often fail to strike a balance. Rotation-based methods, such as those proposed in (Ashkboos et al., 2024; Liu et al., 2024), reduce outliers in both weights and activations through rotation, thereby decreasing the hypercube volume to increase QSUR. As proven in Appendix A.2.2, this ability to reduce outliers stems from the capacity to modify the matrix $\boldsymbol{Q}$, which improves with increasing dimensionality. When the orthogonal matrix is $\boldsymbol{T} = d^{-\frac{1}{2}}\boldsymbol{H}\boldsymbol{Q}^\top$, where d is the dimensionality, and $\boldsymbol{H}$ is a matrix composed of ± 1 entries, the best outlier reduction capability can be achieved.

In combination with Eq7, the maximum QSUR is achieved when:

$$\boldsymbol{T} = c \cdot \boldsymbol{\Lambda}^{-\frac{1}{2}}\boldsymbol{Q}^\top \tag{8}$$

where c is an arbitrary scalar. At this point, the maximum utilization rate is given by $\text{QSUR}'' = \frac{\frac{\pi^{d/2}}{\Gamma(d/2+1)}}{2^d}$. Further details can be found in Appendix A.2.3.

4 METHODOLOGY

4.1 ORTHOGONAL AND SCALING TRANSFORMATION-BASED QUANTIZATION

We propose Orthogonal and Scaling Transformation-based Quantization (OSTQuant), a novel framework designed to optimize the distributions of weights and activations in LLMs through learnable

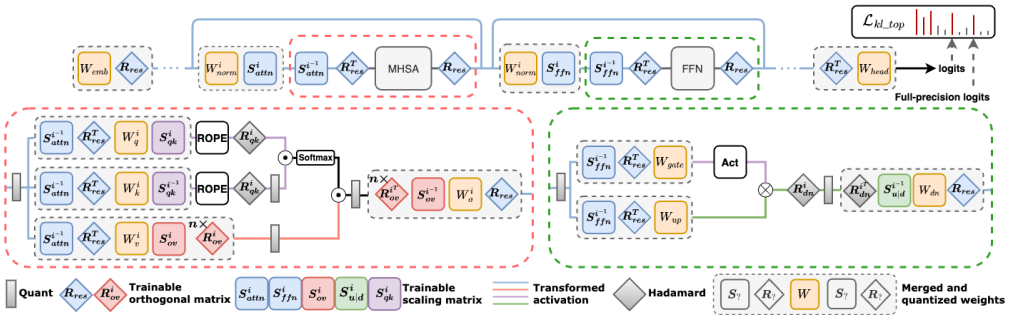

Figure 5: The overall flow diagram of OSTQuant. The top section illustrates how the global orthogonal transformation, $\boldsymbol{R}_{res}$, along with the two scaling transformations, $\boldsymbol{S}_{attn}$ and $\boldsymbol{S}_{ffn}$, collaborate within each block to adjust the distributions across the entire network while maintaining computational invariance. The bottom section highlights four equivalent transformation pairs applied to the FFN and Self-Attention layers. Each fully-connected layer's activation and weight are influenced by one or more of these transformation pairs. During runtime, these transformation pairs are fused with the weights, ensuring minimal runtime overhead.

equivalent transformation pairs, with the goal of improving quantization performance. The core motivation of OSTQuant is that the combination of orthogonal and scaling transformations enhances the QSUR, as illustrated in Fig 1 and explained in Sec 3.

As illustrated in Fig. 5, OSTQuant applies multiple transformation pairs globally within and across blocks of LLMs. Specifically, four equivalent transformation pairs are learned within each block, with each pair consisting of a learnable diagonal scaling matrix and a learnable orthogonal matrix. These transformations work together to reshape the distributions of weights and activations, making them more quantization-friendly. OSTQuant preserves equivalent transformations at a global network level. As a result, the final output of the network remains unchanged when quantization is not applied, effectively preventing overfitting.

Equivalent Transformation Pair We define a transformation pair as $\boldsymbol{T} = \boldsymbol{\Lambda}\boldsymbol{O}$, where $\boldsymbol{T}$ consists of a diagonal scaling matrix $\boldsymbol{\Lambda}$ and a unit orthogonal matrix $\boldsymbol{O}$. As a result, the forward inference process is reformulated as follows:

$$\boldsymbol{y} = \mathcal{Q}(\boldsymbol{x}\boldsymbol{W_1}\boldsymbol{O}\boldsymbol{\Lambda})\mathcal{Q}(\boldsymbol{\Lambda}^{-1}\boldsymbol{O}^T\boldsymbol{W_2}) \tag{9}$$

where $\mathcal{Q}(\cdot)$ represents the quantization operation. Since $\boldsymbol{\Lambda}$ is a diagonal matrix, its inverse is simply the reciprocal of its diagonal elements. We directly optimize $\boldsymbol{O}$ because any orthogonal matrix $\boldsymbol{O}$ can be decomposed into a Hadamard transform and another orthogonal matrix.

Equivalent Transformation Pair has three advantages: **1.** Earnability and Computational Efficiency: Both $\boldsymbol{O}$ and $\boldsymbol{\Lambda}$ are learnable parameters. The inversion of the diagonal matrix $\boldsymbol{\Lambda}$ is computationally simple, enabling efficient forward passes. The orthogonal matrix $\boldsymbol{O}$ can be optimized using gradient-based optimizers, such as RiemannAdam (Bécigneul & Ganea, 2018), which supports optimization on Stiefel Manifolds. This allows the entire process to fully leverage first-order gradient information for end-to-end learning. **2.** Equivalence Preservation: Ignoring the effects of quantization, the forward process remains mathematically equivalent to the original model. This ensures that activations and weights retain their consistency while making their distributions more quantization-friendly, thus reducing the risk of overfitting. **3.** After optimization, $\boldsymbol{O}$ and $\boldsymbol{\Lambda}$ can be directly merged into the existing weights, meaning no additional computational overhead or parameters are introduced during deployment, ensuring efficient inference.

The optimization objective for the entire network can be formalized as:

$$\arg\min_{\boldsymbol{A}_i,\boldsymbol{O}_i} \mathcal{L}(\hat{y}, y; \boldsymbol{A}_i, \boldsymbol{O}_i, \theta) \tag{10}$$

where θ represents the frozen network parameters, and $\mathcal{L}(\hat{y}, y)$ represents the loss between the quantized network output $\hat{y}$ and the full-precision output y.

Weight Outlier Minimization Initialization (WOMI) As shown in (Cholakov et al., 2023), Weight typically follow a Gaussian distribution with zero mean. Therefore, we initialize the orthogonal matrix $\boldsymbol{O}$ using the Eq 27 provided in appendix. For the global orthogonal matrix $\boldsymbol{R}_{res}$, we concatenate the

weights of all linear layers receiving residual inputs along the input channels, denoted as $\boldsymbol{W}^{n \cdot oc \times ic}$, and perform eigenvalue decomposition on its covariance to obtain the eigenmatrix $\boldsymbol{Q_W}$. Then, we initialize $\boldsymbol{R}_{res} = (\boldsymbol{Q_W})\boldsymbol{H}^T$, $\boldsymbol{H}$ is normalized Hadamard matrix. For the orthogonal matrices of the Out-projection and Value-projection layers, we split the $\boldsymbol{O}$ matrix along the head dimension and apply the same initialization method as $\boldsymbol{R}_{res}$. For all scaling matrices, we initialize them as identity matrices.

Inter-Block Learning. As illustrated in the upper half of Fig 5, the global $\boldsymbol{R}_{res}$ is applied at the embedding layer and propagates through each residual path within the LLM via the projection layers. This transformation rotates activations throughout the entire residual path. Due to the norm-preserving property of unitary orthogonal matrices (Tseng et al., 2024), we can bypass the RMSNorm layers and apply an inverse transformation to the inputs of each residual connection's projection layer and the final output head, ensuring equivalence is maintained.

Additionally, for the two normalization layers in each block and their respective projection layers, we introduce two diagonal scaling matrices, $\boldsymbol{S}^i_{attn}$ and $\boldsymbol{S}^i_{ffn}$, to smooth channel-wise differences. The matrix $\boldsymbol{R}_{res}$ simultaneously rotates activations along the residual paths and adjusts the weights of multiple projection layers. The scaling matrices $\boldsymbol{S}^i_{attn}$ and $\boldsymbol{S}^i_{ffn}$ apply scaling to the outputs of the RMSNorm layers and their corresponding projection layers. These transformations can be absorbed into the corresponding weight matrices: the orthogonal transformation $\boldsymbol{R}_{res}$ merges with the projection weights along the residual paths, and the scaling matrices are incorporated into the weight vectors of the RMSNorm layers. As shown in Fig 5, by fusing $\boldsymbol{R}_{res}$ with all projection weights during optimization, we effectively learn how distribution shifts in weights and activations impact model accuracy. This approach helps mitigate the effects of quantization errors by adjusting for these shifts, thus improving model performance.

Intra-Block Learning. As illustrated in the lower half of Fig 5, we introduce two equivalent transformation pairs within the Multi-Head Self-Attention layer of each transformer block. Specifically, the value ($\boldsymbol{V}$) and output ($\boldsymbol{O}$) projection layers are transformed across layers. For each attention head, the data flow is expressed as:

$$\boldsymbol{Y} = \boldsymbol{P}^h \cdot \boldsymbol{X}^h \cdot (\boldsymbol{W}_v^h \boldsymbol{R}_{ov}^h \boldsymbol{S}_{ov}^h) \cdot (\boldsymbol{S}_{ov}^{h^{-1}} \boldsymbol{R}_{ov}^{h^T} \boldsymbol{W}_o^h) \tag{11}$$

Here, h denotes the head index, $\boldsymbol{P}^h$ is the attention matrix, and $\boldsymbol{X}^h$ is the input to head h. We learn a rotation transformation $\boldsymbol{R}_{ov}^h$ and a scaling transformation $\boldsymbol{S}_{ov}^h$ for each attention head. These transformations aim to improve QSUR for both the value cache and the output projection layer.

After the Rotary Positional Encoding (ROPE) operation, the output query and key can naturally undergo an equivalent scaling transformation $\boldsymbol{S}_{qk}$, similar to the approach in (Hu et al., 2024). Due to the multiplicative nature of positional encoding, this scaling transformation can be incorporated into the weight matrices $\boldsymbol{W}_q$ and $\boldsymbol{W}_k$. To further enhance the quantization efficiency of the key cache, we apply an additional Hadamard transformation like Quarot (Ashkboos et al., 2024) to the outputs of the query and key. Similar to $\boldsymbol{S}_{qk}$, we can optimize the diagonal matrices in the up-projection and down-projection of the FFN layer. However, the inverse of the Hadamard transformation is fused into $\boldsymbol{W}_{down}$ from the very beginning.

4.2 KL-Top Loss.

While LLMs are typically trained on vast datasets, OSTQuant optimization is often performed using a much smaller sample set, typically around 1,000 examples. In this limited-data setting, directly applying original cross-entropy (CE) loss can result in accuracy drop. As shown in Tab 1, despite the quantized model exhibiting lower perplexity compared to its full-precision counterpart after training with CE loss, its performance on zero-shot tasks declines. One likely explanation is that small and simple datasets, such as WikiText-2 (Merity

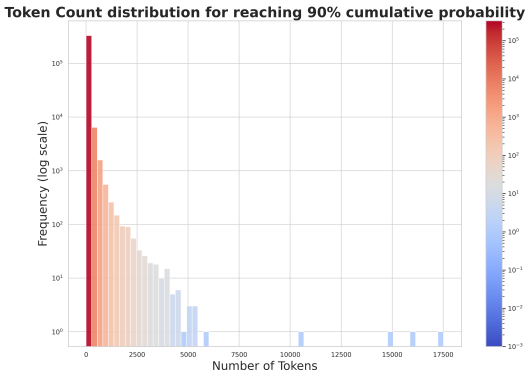

Figure 6: The distribution of the number of tokens required to accumulate 90% of the total prediction probability in the LLaMA-2-7B.

et al., 2016), may not fully utilize the capacity of LLMs. Consequently, relying solely on CE loss, which focuses on a single label, might cause the model to overfit to a narrow set of features, thereby compromising its emergent capabilities.

Table 1: Impact of different loss on Wiki PPL and Arc (Boratko et al., 2018) accuracy for LLaMA models: While Origin loss reduces PPL, zero-shot scores better reflect the model's performance.

Model	Loss Type	Wiki PPL	Arc-Easy Score	Arc-Challenge Score
LLaMA-2-7B	Origin	**5.38**	69.87	42.41
	KL-Top	5.94	**72.69**	**44.62**
LLaMA-2 13B	Origin	**5.12**	75.09	46.08
	KL-Top	5.25	**75.29**	**47.10**
LLaMA-3 8B	Origin	**6.80**	76.68	49.26
	KL-Top	7.29	**76.73**	**49.32**

A natural idea is to align the prediction distributions before and after quantization to reduce overfitting risks, such as using the Kullback-Leibler (KL) divergence for optimization. However, this approach also faces challenges. LLMs typically have vocabularies of tens of thousands or more(e.g., LLaMA-3-8B has over 100,000 tokens). As illustrated in Fig 6, the prediction results of the full-precision model follow a severe long-tail distribution, with only a small number of tokens having significant probabilities. If we directly apply KL divergence over all classes, the loss may be dominated by uninformative classes with negligible probabilities, adding noise to the training process.

To address this, we propose the KL-Top loss function, which computes KL divergence over only the top-k classes with the highest probabilities. By focusing optimization on the model's primary predictions, this approach enhances gradient quality. In the global KL loss, low-probability values can introduce noise, leading to inaccurate gradient updates. By restricting the computation to the top-k classes, the model receives clearer and more informative gradients. Moreover, when dealing with a large number of classes (e.g., over 100,000), both computation and memory costs become substantial. Limiting the calculation to the top-k classes (e.g., k = 1000) not only reduces complexity but also accelerates the training process. The KL-Top loss is calculated as follows:

$$idxs = \text{top}k(\boldsymbol{z}) \tag{12}$$

$$\mathcal{L} = \sum_{i \in idxs} \boldsymbol{z}[i] \log \left(\frac{\boldsymbol{z}[i]}{\hat{\boldsymbol{z}}[i]} \right) \tag{13}$$

where $\boldsymbol{z}$ and $\hat{\boldsymbol{z}}$ are the prediction distributions before and after quantization, respectively.

5 EXPERIMENTS

Models and Datasets. We apply our method to the entire LLaMA family, including LLaMA-1 (7B–30B) (Touvron et al., 2023a), LLaMA-2 (7B–13B) (Touvron et al., 2023b), and LLaMA-3-8B. We report perplexity (PPL) scores on the WikiText2 (Merity et al., 2016) test set. However, as mentioned in Tab 1, perplexity may not fully reflect the model's true performance after quantization, zero-Shot tasks better reflect the model's actual performance. Therefore, we also evaluate the models on up to nine zero-shot tasks using the `lm-evaluation-harness` (version 0.4.4) (Gao et al., 2024), including BoolQ (Clark et al., 2019), HellaSwag (Zellers et al., 2019), LAMBADA (OpenAI) (Radford et al., 2019), OpenBookQA (OBQA) (Mihaylov et al., 2018), PIQA (Bisk et al., 2020), SIQA (Sap et al., 2019), WinoGrande (Sakaguchi et al., 2021), ARC-Easy, and ARC-Challenge (Boratko et al., 2018).

Baselines and Implementation Details. In addition to the basic RTN approach, we benchmark our approach against SmoothQuant (Xiao et al., 2022), GPTQ (Frantar et al., 2022), and current state-of-the-art methods such as Quarot (Ashkboos et al., 2024) and SpinQuant (Liu et al., 2024) for both weight-only and weight-activation quantization. All activations are quantized using per-token asymmetric quantization without any pruning operations, while weights are quantized using symmetric per-channel quantization. We use RiemannAdam (Bécigneul & Ganea, 2018) to optimize all unit orthogonal matrices and scaling matrices. During the distribution optimization phase, we use 1,000 samples from WikiText2, each with a token length of 2,048, and iterate 150 times with a batch size of 8. We apply cosine learning rate decay, setting the initial learning rate for all orthogonal matrix parameters to 2×10^{-2} and for scaling parameters to 3×10^{-2}.

Table 2: Comparison of perplexity on WikiText2 and averaged accuracy on nine Zero-Shot tasks. Results for SmoothQuant, GPTQ, OmniQuant, AWQ, and QuaRot are based on official code and SpinQuant's results for LLaMA-2/3 using official weights, with LLaMA-1 from the official code.

#Bits W-A-KV	Method	LLaMA-3 8B 0-shot[9] Avg.(↑)	LLaMA-3 8B Wiki (↓)	LLaMA-3 70B 0-shot[9] Avg.(↑)	LLaMA-3 70B Wiki (↓)	LLaMA-2 7B 0-shot[9] Avg.(↑)	LLaMA-2 7B Wiki (↓)	LLaMA-2 13B 0-shot[9] Avg.(↑)	LLaMA-2 13B Wiki (↓)	LLaMA-2 70B 0-shot[9] Avg.(↑)	LLaMA-2 70B Wiki (↓)	LLaMA 7B 0-shot[9] Avg.(↑)	LLaMA 7B Wiki (↓)	LLaMA 13B 0-shot[9] Avg.(↑)	LLaMA 13B Wiki (↓)	LLaMA 30B 0-shot[9] Avg.(↑)	LLaMA 30B Wiki (↓)
16-16-16	FloatingPoint	68.09	6.14	73.81	2.86	65.21	5.47	67.61	4.88	71.59	3.32	64.48	5.68	66.67	5.09	70.00	4.10
4-16-16	RTN	63.70	8.13	31.15	1e5	61.27	7.02	60.24	6.39	69.62	3.87	62.67	7.94	63.45	8.60	65.69	6.13
	SmoothQuant	62.79	8.12	67.94	6.70	58.88	8.03	62.03	5.86	65.93	5.50	62.24	7.46	62.69	18.75	65.69	5.80
	GPTQ	61.03	7.43	31.45	9e3	60.86	9.84	64.71	5.79	70.96	3.94	60.15	7.93	64.36	6.58	66.95	5.26
	Omniquant	65.66	7.19	-	-	63.19	5.74	66.38	5.02	71.04	3.47	63.42	5.86	66.22	5.21	69.07	4.25
	AWQ	67.03	7.36	68.92	5.92	63.89	5.83	66.25	5.07	70.88	4.03	63.30	5.97	65.58	5.28	69.44	4.28
	QuaRot	67.27	6.53	72.93	3.53	64.30	5.62	66.95	5.00	71.21	3.41	63.40	5.83	65.91	5.20	69.73	4.27
	SpinQuant	66.54	**6.49**	72.90	3.49	63.59	**5.58**	67.14	5.00	71.12	3.43	63.94	**5.76**	66.32	**5.16**	69.62	4.21
	OSTQuant	**67.80**	6.53	**73.69**	**3.19**	**64.37**	5.64	**67.31**	**4.94**	**71.48**	**3.41**	**64.13**	5.81	**66.62**	5.21	**69.84**	**4.19**
4-4-16	RTN	33.42	6e2	31.21	8e3	32.44	nan	30.86	8e3	30.90	7e4	32.51	7e3	31.63	3e4	31.57	2e3
	SmoothQuant	33.04	1e3	34.67	2e2	32.13	nan	34.26	1e3	35.86	3e2	34.42	3e2	33.29	6e2	34.64	1e3
	GPTQ	32.98	5e2	31.47	4e4	32.72	nan	30.11	4e3	30.86	nan	32.12	1e3	31.51	3e3	30.88	2e3
	QuaRot	61.69	8.02	65.56	6.35	61.87	6.05	65.13	5.35	69.96	3.78	61.76	6.22	64.46	5.50	68.14	4.57
	SpinQuant	64.11	7.28	66.99	6.10	57.37	6.78	63.23	5.24	70.58	3.68	61.82	6.08	64.59	**5.36**	68.08	4.53
	OSTQuant	**65.14**	**7.24**	**72.21**	**3.97**	**63.90**	**5.60**	**66.24**	**5.14**	**70.92**	**3.57**	**62.72**	**6.04**	**65.80**	5.40	**68.52**	**4.43**
4-4-4	RTN	33.18	7e2	30.82	8e3	32.67	nan	30.93	7e3	31.73	7e4	32.87	1e4	31.33	3e4	31.64	2e3
	SmoothQuant	32.96	1e3	33.76	3e2	32.12	nan	33.36	1e3	35.54	3e2	33.32	3e2	33.28	5e2	34.65	1e3
	GPTQ	33.71	6e2	31.20	4e4	33.52	nan	27.85	5e3	31.09	nan	31.80	2e3	30.63	3e3	31.07	2e3
	Omniquant	32.33	4e2	-	-	48.40	14.26	50.35	12.30	-	-	48.46	11.26	45.63	10.87	45.04	12.35
	QuaRot	61.38	8.18	65.33	6.6	61.48	6.11	65.16	5.39	70.30	3.80	61.22	6.26	64.59	5.53	68.08	4.60
	SpinQuant	64.10	7.35	66.31	6.24	62.01	5.96	64.13	5.74	70.57	3.61	61.32	6.12	64.95	**5.39**	68.14	4.55
	OSTQuant	**65.37**	**7.29**	**71.69**	**4.01**	**63.18**	**5.91**	**65.41**	**5.25**	**70.84**	**3.59**	**62.55**	**6.07**	**65.43**	5.40	**68.20**	**4.42**

5.1 Overall Results

Quantization performance. As shown in Tab 2, our method consistently outperforms previous SOTA approaches across almost all configurations and models. Under the 4-16-16 setup, OSTQuant surpasses all prior methods, maintaining at least 99.5% floating-point (FP) accuracy in zero-shot tasks. Compared to other weight-only methods like GPTQ and AWQ, OSTQuant further narrows the gap with FP models. In the most challenging LLaMA-3-8B model, OSTQuant achieves only a 0.29-point performance drop in zero-shot evaluations, whereas other methods incur losses exceeding 1.55 points. Even in the highly challenging 4-4-4 setting, our approach retains a significant performance gain, outperforming the SOTA method, SpinQuant, by around 1 point across multiple models. Notably, when the KV cache is not quantized (in the 4-4-16 setup), OSTQuant achieves a significant performance boost over SpinQuant, with gains up to 6.53 points (LLaMA-2 7B). These substantial performance improvements demonstrate the effectiveness of our approach. More detailed results can be seen in Appendix A.6. Once activation is quantized, rotation-based methods significantly outperform smooth-based methods, confirming that latter struggle with outliers and uneven distributions. In Fig 3, the QSUR across different methods show a clear positive correlation with model performance. Our approach achieves the highest QSUR, effectively mitigating the challenges of outliers and uneven distributions that hinder prior methods, leading to improved model accuracy.

Table 3: The speedup and memory saving factor of LLaMA models with different parameter sizes and sequence lengths, compared between our 4-bit implementation and FP16. All tests were conducted on a Transformer block with batch size 4 on a 3090 GPU.

Model Size	Prefill Speedup (Seqlen)						Memory Saving Factor (Seqlen)					
	256	**512**	**1024**	**2048**	**4096**	**8192**	**256**	**512**	**1024**	**2048**	**4096**	**8192**
7B	2.24x	2.27x	2.23x	2.14x	2.11x	2.02x	3.48x	3.34x	3.12x	2.86x	2.57x	2.34x
8B	2.42x	2.52x	2.52x	2.43x	2.36x	2.23x	3.48x	3.36x	3.12x	2.77x	2.38x	2.00x
13B	2.62x	2.68x	2.63x	2.52x	2.83x	2.32x	3.64x	3.51x	3.30x	3.02x	2.70x	2.43x
30B	3.18x	3.01x	2.98x	3.40x	2.84x	2.68x	3.70x	3.59x	3.42x	3.15x	2.83x	2.53x

Speedup and memory savings. OSTQuant incurs only negligible loss in 4-bit quantization, making 4-bit inference feasible. As shown in Tab 3, OSTQuant delivers an average inference speedup of over $2\times$ and memory savings exceeding $3.5\times$, demonstrating the significant improvements in inference efficiency. Detailed speedup and memory saving results can refer to Tab 9. Moreover, OSTQuant provides substantial advantages in training speed compared to block reconstruction-based methods. With only 150 iterations and a minimal number of learnable parameters, we optimize the 7B and 13B models in around 20 minutes, and the 30B model in 120 minutes, achieving up to $5.3\times$ speedups compared to OmniQuant, refer to Tab 11 for more details.

5.2 Ablation Study

Effect of different transformation. We ablate the effects of various transformation matrices on LLaMA-2 7B, identifying four groups where orthogonal and scaling equivalent transformations can

Table 4: Ablation study on the impact of different transformation matrices on Wiki PPL and zero-shot[9] score for LLaMA-2 7B under W4A4KV4 quantization.

Metric	Baseline	$+\boldsymbol{R}_{res}$	$+\boldsymbol{S}_{res}$	$+\boldsymbol{R}_{dn}$	$+\boldsymbol{S}_{u\|d}$	$+\boldsymbol{R}_{qk}$	$+\boldsymbol{S}_{qk}$	$+\boldsymbol{R}_{ov}$	$+\boldsymbol{S}_{ov}$
Wiki PPL	nan	9.70	9.46	6.16	6.00	5.92	5.92	5.94	**5.91**
Zero-shot[9]	33.51	54.33	53.74	61.75	61.79	62.35	62.56	63.11	**63.18**

be applied. Tab 4 presents the contribution of each parameter group under W4A4KV4 setup. Our results show that the global orthogonal transformation $\boldsymbol{R}_{res}$ brings the largest improvement, followed closely by $\boldsymbol{R}_{down}$. Notably, scaling transformations $\boldsymbol{S}$ further build on the orthogonal transformations $\boldsymbol{R}$ by effectively balancing variance across channels, thereby minimizing quantization losses and enhancing model performance.

Table 5: Effect of different optimizers on zero-shot[9] performance of LLaMA models under the W4A4KV4 configuration. LR1 and LR2 represent the learning rates for the scaling matrices and unitary orthogonal matrices.

Model	Optimizer Type	Best Steps	Best LR1	Best LR2	Zero-Shot[9] Score
LLaMA-2-7B	Cayley SGD	150	1.50	0.20	63.11
	Riemann SGD	500	0.10	0.02	63.09
	Riemann Adam	150	0.02	1e-3	**63.18**
LLaMA-2-13B	Cayley SGD	200	1.50	0.2	64.77
	Riemann SGD	500	0.1	0.02	65.19
	Riemann Adam	150	0.02	0.002	**65.41**

Different Manifold Optimizers. Since the unit orthogonal matrix resides on a Stiefel manifold, we explore various manifold optimizers to optimize it, including CayleySGD (Li et al., 2020), RiemannSGD, and RiemannAdam (Bécigneul & Ganea, 2018). Tab 5 compares these methods and shows that CayleySGD typically requires a higher learning rate to perform well, RiemannSGD needs more iterations, while RiemannAdam delivers the best results with the fewest iterations. We also discover that using a learning rate for the Stiefel manifold 10 times larger than that for scaling transformation parameters leads to better results.

Table 6: Ablation study of k values on Zero-Shot[9] score and Wiki PPL for W3-only and W4A4KV4 configurations of LLaMA-2 7B.

Setting	Metric	k=5	k=50	k=100	k=500	k=1000	k=5000	k=10000
W3 Only	Zero-Shot[9] Score	61.87	61.88	61.75	62.18	**62.30**	61.25	61.21
	Wiki PPL	6.06	6.116	6.13	6.07	**6.06**	6.06	6.12
W4A4KV4	Zero-Shot[9] Score	62.4	62.13	62.38	62.34	**63.18**	62.44	62.11
	Wiki PPL	5.99	5.96	5.95	5.96	5.96	**5.93**	5.94

Influence of k in KL-Top loss. The parameter k in Eq. 12 defines the number of classes considered when calculating the KL-Top loss, balancing optimization difficulty with semantic richness. Both excessively large or small k values negatively impact optimization. Tab 6 shows a comparison of different k values. Furthermore, we analyze whether to apply softmax before or after the top-k selection. Our experiments indicate that setting k to 1,000 processing produces the best outcomes.

6 Conclusion

In this paper, we introduce OSTQuant, a novel post-training quantization method designed to enhance the efficiency of large language models (LLMs). Central to OSTQuant is the Quantization Space Utilization Rate (QSUR), a new metric we proposed to effectively assess the quantizability of transformed data by measuring its space utilization within the quantization space. Complemented by mathematical derivations, QSUR provides theoretical guidance for optimizing single data distributions across the entire quantization space. Leveraging this insight, OSTQuant employs a learnable equivalent transformation pair composed of orthogonal and scaling transformations to optimize the distributions of weights and activations. Additionally, we introduce the KL-Top loss function to mitigate noise during optimization while retaining richer semantic information, even with the limited calibration data typically available in PTQ. Extensive experiments on various LLMs and benchmarks demonstrate that OSTQuant outperforms existing quantization methods. These results highlight the effectiveness of optimizing data distributions across the quantization space and underscore OSTQuant's potential to advance LLM quantization, making these models more efficient and practical for deployment in resource-constrained environments.

REFERENCES

Josh Achiam, Steven Adler, Sandhini Agarwal, Lama Ahmad, Ilge Akkaya, Florencia Leoni Aleman, Diogo Almeida, Janko Altenschmidt, Sam Altman, Shyamal Anadkat, et al. Gpt-4 technical report. *arXiv preprint arXiv:2303.08774*, 2023.

Saleh Ashkboos, Amirkeivan Mohtashami, Maximilian L Croci, Bo Li, Martin Jaggi, Dan Alistarh, Torsten Hoefler, and James Hensman. Quarot: Outlier-free 4-bit inference in rotated llms. *arXiv preprint arXiv:2404.00456*, 2024.

Gary Bécigneul and Octavian-Eugen Ganea. Riemannian adaptive optimization methods. *arXiv preprint arXiv:1810.00760*, 2018.

Yonatan Bisk, Rowan Zellers, Jianfeng Gao, Yejin Choi, et al. Piqa: Reasoning about physical commonsense in natural language. In *Proceedings of the AAAI conference on artificial intelligence*, volume 34, pp. 7432–7439, 2020.

Michael Boratko, Harshit Padigela, Divyendra Mikkilineni, Pritish Yuvraj, Rajarshi Das, Andrew McCallum, Maria Chang, Achille Fokoue-Nkoutche, Pavan Kapanipathi, Nicholas Mattei, et al. A systematic classification of knowledge, reasoning, and context within the arc dataset. *arXiv preprint arXiv:1806.00358*, 2018.

Jerry Chee, Yaohui Cai, Volodymyr Kuleshov, and Christopher De Sa. Quip: 2-bit quantization of large language models with guarantees. *arXiv preprint arXiv:2307.13304*, 2023.

Long Chen, Oleg Sinavski, Jan Hünermann, Alice Karnsund, Andrew James Willmott, Danny Birch, Daniel Maund, and Jamie Shotton. Driving with llms: Fusing object-level vector modality for explainable autonomous driving. In *2024 IEEE International Conference on Robotics and Automation (ICRA)*, pp. 14093–14100. IEEE, 2024.

Radostin Cholakov, Han Guo, and Yoon Kim. Distributional quantization of large language models. *cee org*, 2023.

Christopher Clark, Kenton Lee, Ming-Wei Chang, Tom Kwiatkowski, Michael Collins, and Kristina Toutanova. Boolq: Exploring the surprising difficulty of natural yes/no questions. *arXiv preprint arXiv:1905.10044*, 2019.

Tim Dettmers, Mike Lewis, Younes Belkada, and Luke Zettlemoyer. Gpt3. int8 (): 8-bit matrix multiplication for transformers at scale. *Advances in Neural Information Processing Systems*, 35: 30318–30332, 2022.

Elias Frantar, Saleh Ashkboos, Torsten Hoefler, and Dan Alistarh. Gptq: Accurate post-training quantization for generative pre-trained transformers. *arXiv preprint arXiv:2210.17323*, 2022.

Leo Gao, Jonathan Tow, Baber Abbasi, Stella Biderman, Sid Black, Anthony DiPofi, Charles Foster, Laurence Golding, Jeffrey Hsu, Alain Le Noac'h, Haonan Li, Kyle McDonell, Niklas Muennighoff, Chris Ociepa, Jason Phang, Laria Reynolds, Hailey Schoelkopf, Aviya Skowron, Lintang Sutawika, Eric Tang, Anish Thite, Ben Wang, Kevin Wang, and Andy Zou. A framework for few-shot language model evaluation, 07 2024. URL `https://zenodo.org/records/12608602`.

Xing Hu, Yuan Chen, Dawei Yang, Sifan Zhou, Zhihang Yuan, Jiangyong Yu, and Chen Xu. I-llm: Efficient integer-only inference for fully-quantized low-bit large language models. *arXiv preprint arXiv:2405.17849*, 2024.

Ioan Mackenzie James. *The topology of Stiefel manifolds*, volume 24. Cambridge University Press, 1976.

Diederik P Kingma. Adam: A method for stochastic optimization. *arXiv preprint arXiv:1412.6980*, 2014.

Max Kochurov, Rasul Karimov, and Serge Kozlukov. Geoopt: Riemannian optimization in pytorch, 2020.

Changhun Lee, Jungyu Jin, Taesu Kim, Hyungjun Kim, and Eunhyeok Park. Owq: Lessons learned from activation outliers for weight quantization in large language models. *arXiv preprint arXiv:2306.02272*, 2023.

Jun Li, Li Fuxin, and Sinisa Todorovic. Efficient riemannian optimization on the stiefel manifold via the cayley transform. *arXiv preprint arXiv:2002.01113*, 2020.

Ji Lin, Jiaming Tang, Haotian Tang, Shang Yang, Xingyu Dang, and Song Han. Awq: Activation-aware weight quantization for llm compression and acceleration. *arXiv preprint arXiv:2306.00978*, 2023.

Zechun Liu, Changsheng Zhao, Igor Fedorov, Bilge Soran, Dhruv Choudhary, Raghuraman Krishnamoorthi, Vikas Chandra, Yuandong Tian, and Tijmen Blankevoort. Spinquant–llm quantization with learned rotations. *arXiv preprint arXiv:2405.16406*, 2024.

Yuexiao Ma, Huixia Li, Xiawu Zheng, Feng Ling, Xuefeng Xiao, Rui Wang, Shilei Wen, Fei Chao, and Rongrong Ji. Affinequant: Affine transformation quantization for large language models. *arXiv preprint arXiv:2403.12544*, 2024.

Stephen Merity, Caiming Xiong, James Bradbury, and Richard Socher. Pointer sentinel mixture models. *arXiv preprint arXiv:1609.07843*, 2016.

Todor Mihaylov, Peter Clark, Tushar Khot, and Ashish Sabharwal. Can a suit of armor conduct electricity? a new dataset for open book question answering. *arXiv preprint arXiv:1809.02789*, 2018.

Alec Radford, Jeffrey Wu, Rewon Child, David Luan, Dario Amodei, Ilya Sutskever, et al. Language models are unsupervised multitask learners. *OpenAI blog*, 1(8):9, 2019.

Keisuke Sakaguchi, Ronan Le Bras, Chandra Bhagavatula, and Yejin Choi. Winogrande: An adversarial winograd schema challenge at scale. *Communications of the ACM*, 2021.

Maarten Sap, Hannah Rashkin, Derek Chen, Ronan LeBras, and Yejin Choi. Socialiqa: Commonsense reasoning about social interactions. *arXiv preprint arXiv:1904.09728*, 2019.

Wenqi Shao, Mengzhao Chen, Zhaoyang Zhang, Peng Xu, Lirui Zhao, Zhiqian Li, Kaipeng Zhang, Peng Gao, Yu Qiao, and Ping Luo. Omniquant: Omnidirectionally calibrated quantization for large language models. *CoRR*, abs/2308.13137, 2023.

Hugo Touvron, Thibaut Lavril, Gautier Izacard, Xavier Martinet, Marie-Anne Lachaux, Timothée Lacroix, Baptiste Rozière, Naman Goyal, Eric Hambro, Faisal Azhar, et al. Llama: Open and efficient foundation language models. *arXiv preprint arXiv:2302.13971*, 2023a.

Hugo Touvron, Louis Martin, Kevin Stone, Peter Albert, Amjad Almahairi, Yasmine Babaei, Nikolay Bashlykov, Soumya Batra, Prajjwal Bhargava, Shruti Bhosale, et al. Llama 2: Open foundation and fine-tuned chat models. *arXiv preprint arXiv:2307.09288*, 2023b.

Albert Tseng, Jerry Chee, Qingyao Sun, Volodymyr Kuleshov, and Christopher De Sa. Quip#: Even better llm quantization with hadamard incoherence and lattice codebooks. *arXiv preprint arXiv:2402.04396*, 2024.

Guangxuan Xiao, Ji Lin, Mickael Seznec, Julien Demouth, and Song Han. Smoothquant: Accurate and efficient post-training quantization for large language models. *arXiv preprint arXiv:2211.10438*, 2022.

Zhewei Yao, Reza Yazdani Aminabadi, Minjia Zhang, Xiaoxia Wu, Conglong Li, and Yuxiong He. Zeroquant: Efficient and affordable post-training quantization for large-scale transformers. *arXiv preprint arXiv:2206.01861*, 2022.

Rowan Zellers, Ari Holtzman, Yonatan Bisk, Ali Farhadi, and Yejin Choi. Hellaswag: Can a machine really finish your sentence? *arXiv preprint arXiv:1905.07830*, 2019.

A APPENDIX

A.1 QUANTIZATION PRELIMINARIES

Quantization & Dequantization. Quantization typically refers to mapping a floating-point number to a discrete interval with integer number. Here, we only consider uniform quantization. The quantization process can be expressed as follows:

$$\boldsymbol{X}^I = \text{clamp}\left(\left\lfloor \frac{\boldsymbol{X}}{s} \right\rceil + zp^I, 0, 2^{n^I} - 1\right) \tag{14}$$

$$s = \frac{x_{\max} - x_{\min}}{2^{n^I} - 1} \tag{15}$$

$$zp^I = \left\lfloor \frac{-x_{\min}}{s} \right\rceil \tag{16}$$

$$\boldsymbol{X'} = (\boldsymbol{X}^I - zp^I) \cdot s \tag{17}$$

where $\boldsymbol{X}$ is the floating-point tensor, $\boldsymbol{X^I}$ is its quantized counterpart and $\boldsymbol{X'}$ is the dequantized resuls of $\boldsymbol{X^I}$. Here, n^I represents the number of bits (e.g., 8). s is the quantization step size, determined by $x_{\min}$, $x_{\max}$, and n^I.clamp represents truncation function. The choice of s greatly affects the accuracy of the quantized model. We can obtain s from the activations of some samples, which is called static quantization. Alternatively, we can derive it from runtime statistics, known as dynamic quantization. Quantization can also be distinguished by its granularity into per-channel quantization and per-token quantization (Yao et al., 2022).

A.2 SOME DEDUCTIONS ABOUT QSUR

A.2.1 THE COORDINATES OF THE EXTREMUM POINT AND THE INFLUENCE OF ROTATION MATRIX

From Eq6:

$$\text{QSUR}_X = \frac{V_X}{V_{S_X}} = \frac{\frac{\pi^{d/2}}{\Gamma(d/2+1)} \cdot \left(\chi_d^2(\alpha)\right)^{d/2} \cdot \sqrt{\det(\boldsymbol{\Lambda})}}{\left(\max(\sqrt{\chi_d^2(\alpha) \cdot \lambda_{\max}} \cdot |\boldsymbol{q}_{\max}| + \boldsymbol{\mu}) - \min(\sqrt{\chi_d^2(\alpha) \cdot \lambda_{\min}} \cdot |\boldsymbol{q}_{\min}| + \boldsymbol{\mu})\right)^d}$$

Given that the eigenvalues and the mean vector are fixed, the volume of the hypercube is determined by the eigenmatrix $\boldsymbol{Q}$. For any eigenvector $\boldsymbol{q}i \in \boldsymbol{Q}$, we have the condition:

$$qi1^2 + q_{i2}^2 + \cdots + q_{id}^2 = 1 \tag{18}$$

Let $q_{i\max} = \max(q_{i1}, q_{i2}, \ldots, q_{id})$, which implies that for any i, we have $q_{ij} \leq q_{i\max}$. Therefore, it follows that:

$$q_{i1}^2 + q_{i2}^2 + \cdots + q_{id}^2 \leq d \cdot q_{i\max}^2 \tag{19}$$

This yields the inequality:

$$1 \leq d \cdot q_{i\max}^2 \tag{20}$$

$$|q_{i\max}| \geq d^{\frac{1}{2}} \tag{21}$$

Consequently, when all elements in $\boldsymbol{Q}$ are $\pm d^{-\frac{1}{2}}$, the quantization range is minimized. Under these conditions, the QSUR$'$ can be expressed as:

$$\text{QSUR}' = \frac{\frac{\pi^{d/2}}{\Gamma(d/2+1)} \cdot \left(\chi_d^2(\alpha)\right)^{d/2} \cdot \sqrt{\det(\boldsymbol{\Lambda})}}{\left(\max\left(\sqrt{\chi_d^2(\alpha) \cdot \lambda_{\max}} \cdot d^{-\frac{1}{2}} + \boldsymbol{\mu}\right) - \min\left(-\sqrt{\chi_d^2(\alpha) \cdot \lambda_{\min}} \cdot d^{-\frac{1}{2}} + \boldsymbol{\mu}\right)\right)^d} \tag{22}$$

When the mean vector $\boldsymbol{\mu} = 0$, the QSUR$'$ can be further simplified to:

$$\text{QSUR}' = \frac{\frac{\pi^{d/2}}{\Gamma(d/2+1)} \cdot \sqrt{\prod_{i=1}^d \lambda_i}}{2^d \cdot \left(\sqrt{\lambda_1} \cdot d^{-\frac{1}{2}}\right)^d} \tag{23}$$

A.2.2 THE BEST ORTHOGONAL MATRIX

In the linear transformation paragraph 3 of Sec3 , we observe that applying a linear transformation $\boldsymbol{T}$ to $X \sim \mathcal{N}(\boldsymbol{\mu}, \boldsymbol{\Sigma})$ results in a transformed distribution:

$$\hat{X} \sim \mathcal{N}(\hat{\boldsymbol{\mu}}, \hat{\boldsymbol{\Sigma}}) \tag{24}$$

Since the transformation $\boldsymbol{TQ}$ remains an orthonormal matrix after applying the unitary transformation, the transformed eigenvectors are given by:

$$\mathbf{TQ} = [\mathbf{q_1}, \mathbf{q_2}, \ldots, \mathbf{q_d}] \tag{25}$$

Movited by Eq 21, we aim for the following transformation:

$$\boldsymbol{TQ} = d^{-\frac{1}{2}}\boldsymbol{H} \tag{26}$$

where d is the dimensionality, and $\boldsymbol{H}$ is a matrix composed of ± 1 entries. Solving for $\boldsymbol{T}$ yields:

$$\boldsymbol{T} = d^{-\frac{1}{2}}\boldsymbol{HQ}^\top \tag{27}$$

The covariance matrix after transformation becomes:

$$\hat{\boldsymbol{\Sigma}} = d^{-\frac{1}{2}} \cdot \boldsymbol{HQ}^\top\boldsymbol{Q\Lambda Q}^\top\boldsymbol{QH}^\top \cdot d^{-\frac{1}{2}} \tag{28}$$

$$= d^{-1}\boldsymbol{H\Lambda H}^\top \tag{29}$$

A.2.3 THE BEST TRANSFORM MATRIX

Inspired by Sec 3, we know that applying a linear transformation $\boldsymbol{T}$ to $X \sim \mathcal{N}(\boldsymbol{\mu}, \boldsymbol{\Sigma})$ results in a transformed $\hat{X} \sim \mathcal{N}(\hat{\boldsymbol{\mu}}, \hat{\boldsymbol{\Sigma}})$. Ignoring the mean vector, we present a transformation matrix, composed of a diagonal scaling transformation and an orthonormal transformation, which minimizes the QSUR:

$$\boldsymbol{T} = \boldsymbol{\Lambda}^{-\frac{1}{2}}\boldsymbol{Q}^\top \tag{30}$$

Under this transformation, the covariance matrix becomes:

$$\hat{\boldsymbol{\Sigma}} = \boldsymbol{\Lambda}^{-\frac{1}{2}}\boldsymbol{Q}^\top\boldsymbol{Q\Lambda Q}^\top\boldsymbol{Q\Lambda}^{-\frac{1}{2}} \tag{31}$$

$$= \boldsymbol{I} \tag{32}$$

By substituting this result into Eq 7, we achieve the maximum QSUR:

$$\text{QSUR}'' = \frac{\frac{\pi^{d/2}}{\Gamma(d/2+1)}}{2^d} \tag{33}$$

A.3 ADDITIONAL ABLATION EXPERIMENTS

A.3.1 THE EFFECT OF WEIGHT OUTLIER MINIMIZATION INITIALIZATION

Weight Outlier Minimization Initialization(WOMI) is used to initialize trainable orthogonal matrices. This approach not only reduces outliers in the weights but also leverages the properties of Hadamard matrices to mitigate inter-channel disparities in activations, thereby improving the initial QSUR for both weights and activations.

We visualized the impact of WOMI on the weights. As shown in Fig 7, the original weight distribution exhibits significant variations across input and output channels. While QuaRot reduces inter-channel differences, noticeable spikes remain. WOMI, by leveraging the Hadamard matrix and the covariance matrix of the weight distribution, further smooths these inter-channel differences, effectively reducing the quantization space and relative quantization error. Additional visual results for other layers are presented in Fig 13.

We conducted additional experiments to investigate the impact of WOMI on the performance of quantized models. Tab 7 presents the performance of LLaMA-2-7B and LLaMA-3-8B models initialized with WOMI and random Hadamard matrices. WOMI achieves lower perplexity and higher few-shot accuracy under both W4A4KV4 and W4A16KV16 configurations, showcasing its effectiveness. Interestingly, WOMI demonstrates greater performance improvements in W4-only quantization settings compared to W4A4KV4. This is likely due to WOMI's superior capability in minimizing weight quantization errors, which is especially critical in W4-only configurations.

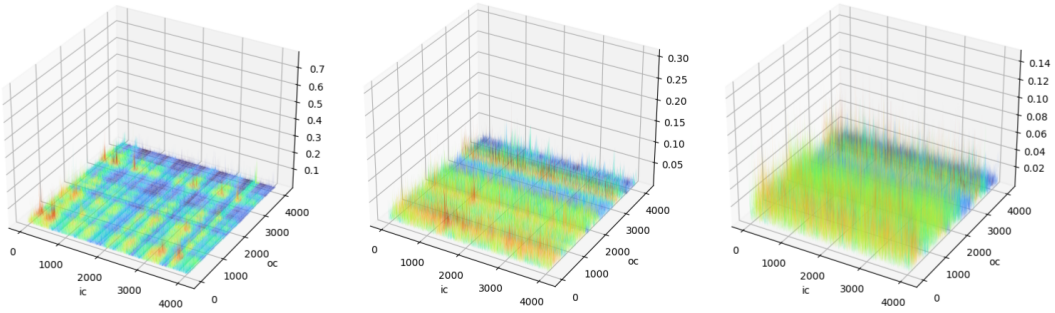

(a) Original weight distribution (b) Hadamard. Relative L1 Error: 0.79 (c) WOMI. Relative L1 Error: 0.42

Figure 7: Impact of WOMI transform and Hadamard transform on LLaMA-2-7B weight (weight of Query projection in Layer 0) quantization. The relative error is computed by dividing the mean absolute error (MAE) between the original and quantized weights by the mean absolute value of the original weights.

Table 7: Comparison of the impact of WOMI initialization and Hadamard initialization on the performance of quantized models.

Model	Quant Setting	Method	Zero-Shot[9]	Wiki PPL
LLaMA-2-7B	Full-Precision	-	65.21	5.47
	W4A16KV16	Hadamard	63.32	5.62
	W4A16KV16	WOMI	63.45	5.59
	W4A4KV4	Hadamard	61.47	6.11
	W4A4KV4	WOMI	61.52	6.09
LLaMA-3-8B	Full-Precision	-	68.09	6.14
	W4A16KV16	Hadamard	67.27	6.53
	W4A16KV16	WOMI	67.41	6.48
	W4A4KV4	Hadamard	61.38	8.18
	W4A4KV4	WOMI	61.40	8.17

A.3.2 The effect of KL-Top Loss

As shown in Tab 8 , the results indicate that using SpinQuant(Liu et al., 2024) alone, even with the introduction of the KL-Top loss function, does not lead to significant performance improvements and may even cause some degradation. However, when combined with orthogonal and scaling transformation pairs, the quantization performance improves significantly. For OSTQuant, using CE loss results in overfitting on the calibration set, and this issue is alleviated by the introduction of the KL-Top loss function.

A.4 Inference Efficiency and Quantization Overhead

Tab 9 shows the prefill time and memory usage of LLaMA models with different parameter sizes and sequence lengths, compared between our 4-bit implementation and FP16. The inference environment features an Intel(R) Xeon(R) Gold 5317 CPU and an Nvidia 3090 GPU. The 4-bit matrix multiplication kernel was implemented using cutlass of nvidia, while the self-attention mechanism was realized with PyTorch's native SDPA (scaled dot product attention) function. All tests were conducted 500 times, with the median value taken as the final result. Benefiting from efficient low-precision computation units within CUDA cores and reduced access overhead, OSTQuant achieves over 2× speedup across various model sizes, and approximately 3× acceleration on the challenging LLaMA-30B model.

Fig 8 displays the performance and model size of various LLaMA models under different quantization bitwidths. Each line represents a different model (LLaMA-2-7B, LLaMA-3-8B, LLaMA-2-13B, LLaMA-30B, and LLaMA-3-70B) with quantization bitwidths ranging from 2 bits to 16 bits. As

Table 8: Performance of SpinQuant with the introduction of the KL-Top loss function on 9 zero-shot dataset tasks and the Perplexity changes on Wikitext2.

Model	Method	ARC-c	ARC-e	BoolQ	HellaS	Lam.	OBQA	PIQA	SIQA	WinoG.	Avg.	Wiki2 PPL
LLaMA3-8B	RTN	23.72	30.56	46.18	29.83	2.70	28.60	52.45	34.39	50.20	33.18	704.34
	SpinQuant	46.33	73.57	76.15	75.43	71.40	41.40	79.16	44.68	68.75	64.10	7.35
	SpinQuant + KL-Top	47.29	73.95	75.82	75.64	71.40	41.58	78.16	44.38	68.45	64.07	7.54
	OSTQuant	49.26	76.68	78.25	76.18	70.48	43.19	77.85	45.18	69.13	65.13	6.80
	OSTQuant + KL-Top	49.32	76.73	78.87	76.01	70.77	43.20	78.51	45.70	69.22	65.37	7.29
LLaMA2-7B	RTN	27.22	27.06	50.83	27.34	0.93	25.80	49.51	34.85	50.51	32.67	nan
	SpinQuant	40.44	71.08	74.40	73.51	70.66	41.80	76.88	43.50	65.82	62.01	5.96
	SpinQuant + KL-Top	40.76	71.29	74.61	73.08	70.19	40.94	76.32	43.85	67.78	62.09	6.16
	OSTQuant	42.41	69.87	75.07	72.90	70.21	40.87	78.16	44.16	68.40	62.45	5.38
	OSTQuant + KL-Top	44.62	72.69	75.41	73.27	70.21	41.00	78.13	44.42	68.27	63.11	5.94

Table 9: Prefill time and Memory usage of LLaMA models with different parameter sizes and sequence lengths, compared between our 4-bit implementation and FP16. All tests were conducted on a Transformer block with batch size 4 on a 3090 GPU.

Model	Seqlen	Prefill Time		Prefill Speedup	Memory		Memory Saving
		FP16	INT4		FP16	INT4	
LLaMA2-7B	256	8.050ms	3.597ms	2.238x	0.411GB	0.118GB	3.479x
	512	14.904ms	6.579ms	2.265x	0.435GB	0.130GB	3.341x
	1024	27.989ms	12.582ms	2.225x	0.483GB	0.155GB	3.116x
	2048	54.276ms	25.312ms	2.144x	0.577GB	0.202GB	2.857x
	4096	112.230ms	53.145ms	2.112x	0.766GB	0.299GB	2.566x
	8192	244.675ms	121.339ms	2.016x	1.147GB	0.491GB	2.336x
LLaMA3-8B	256	8.035ms	3.314ms	2.424x	0.430GB	0.124GB	3.478x
	512	15.545ms	6.176ms	2.517x	0.442GB	0.132GB	3.356x
	1024	29.169ms	11.599ms	2.515x	0.466GB	0.149GB	3.116x
	2048	57.470ms	23.631ms	2.432x	0.513GB	0.185GB	2.774x
	4096	117.523ms	49.835ms	2.358x	0.608GB	0.256GB	2.378x
	8192	256.394ms	114.815ms	2.233x	0.795GB	0.397GB	2.003x
LLaMA2-13B	256	11.449ms	4.370ms	2.620x	0.634GB	0.174GB	3.643x
	512	21.195ms	7.924ms	2.675x	0.663GB	0.189GB	3.512x
	1024	41.752ms	15.867 ms	2.631x	0.723GB	0.219GB	3.301x
	2048	81.965ms	32.553ms	2.518x	0.841GB	0.279GB	3.018x
	4096	199.046ms	70.442ms	2.826x	1.079GB	0.399GB	2.702x
	8192	359.409ms	154.640ms	2.324x	1.551GB	0.639GB	2.426x
LLaMA-30B	256	18.682ms	5.883ms	3.175x	1.047GB	0.283GB	3.703x
	512	34.393ms	11.445ms	3.005x	1.085GB	0.302GB	3.589x
	1024	66.880ms	22.464ms	2.977x	1.162GB	0.340GB	3.416x
	2048	157.500ms	46.317ms	3.400x	1.315GB	0.418GB	3.148x
	4096	272.355ms	96.052ms	2.835x	1.625GB	0.575GB	2.828x
	8192	576.555ms	215.27ms	2.678x	2.242GB	0.887GB	2.527x

we can see, quantizing the weights to below 4 bits leads to a significant drop in accuracy. Another notable observation is that larger models, such as LLaMA-3-70B, outperform smaller floating-point models like LLaMA-30B in both accuracy and parameter size after quantization.

As shown in Tab 10, since the decoding stage of LLMs is often memory-bound, quantizing the weights to 4-bit significantly reduces memory access overhead, thereby accelerating the inference process. The results demonstrate that, under the premise of achieving nearly lossless accuracy, even a single A6000 GPU can successfully run LLaMA-3-70B at a speed of 15 tokens per second after quantization. This validates the effectiveness of our quantization method.

Tab 11 presents a comparison of training time between our approach and block reconstruction-based methods across models of varying parameter sizes. Thanks to the effectiveness of Weight Outlier Minimization Initialization and KL-Top Loss, we require only about 150 iterations to complete the quantization process. As shown in the table, OSTQuant offers a significant optimization speed advantage for smaller models, such as achieving more than a 5x speedup on the LLaMA 7B model compared to OmniQuant. Even for large-scale models like LLaMA 70B, it achieves nearly a 2x speed improvement.

Table 10: Comparison of generation speed and memory usage before and after quantization in the decoding stage.

Model	Decoder Speed (tokens/sec)			Memory Use (GB)		Memory Saving
	FP	Quantized	Speed up	FP	Quantized	
LLaMA-2-7B	47.32	89.4	1.89x	13.94	4.32	3.23x
LLaMA-3-8B	38.33	77.71	2.03x	15.83	5.88	2.69x
LLaMA-2-13B	23.7	55.35	2.34x	23.7	8.5	2.79x
LLaMA-30B	OOM	30.49	-	OOM	18.19	-
LLaMA-3-70B	OOM	14.68	-	OOM	38.41	-

Table 11: Comparison of the training time between our approach and block reconstruction-based methods across models with varying parameter sizes.

Method	7B	8B	13B	30B	70B
Omniquant	1.6h	1.8h	3.3h	7.3h	9.5h
OSTQuant	0.3h	0.4h	0.8h	2.2h	5.5h
Speedup	5.3x	4.5x	4.1x	3.3x	1.7x

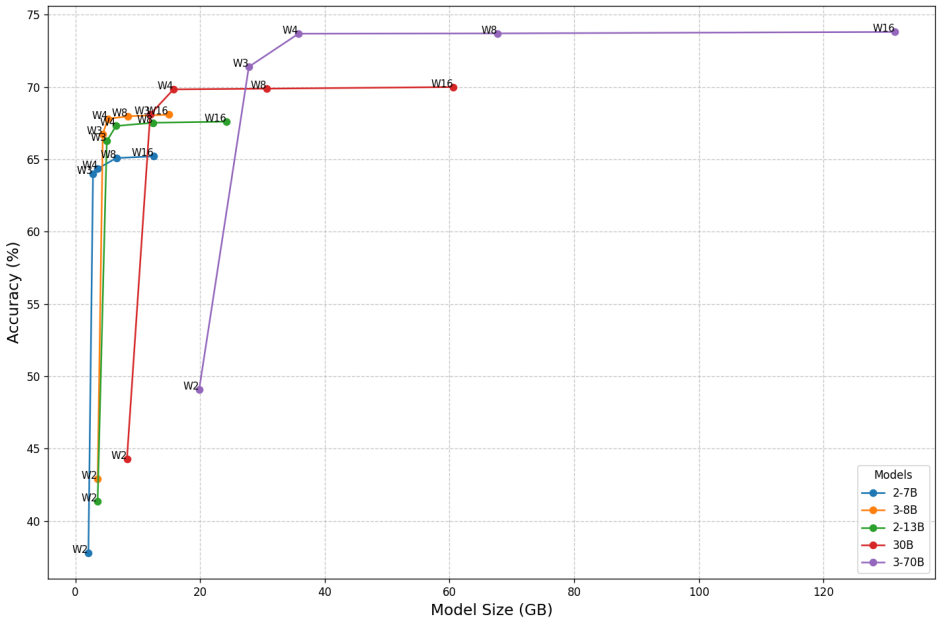

Figure 8: Performance and model size of the Llama series under different quantization settings. Accuracy is calculated by the average score of nine zero-shot datasets. Model size is determined by the memory usage when stored in fp16 or integer formats.

A.5 Future Work

A.5.1 OSTQuant for Fully-Quant Large Language Models

Fig 9 introduces OSTQuant's novel strategy designed for full quantization. Full quantization involves quantizing all activations within each Transformer Block to low bits (as shown by the quantization nodes inserted for all node inputs and outputs in the figure). This reduces memory transfer overhead for activations and fully utilizes efficient low-precision computational units.

As shown in Fig 9, OSTQuant introduces numerous equivalence transformations to alter the distributions of all node input and output activations. Unlike the methods in Fig 5 designed for traditional quantization, the design for fully quantization adds more equivalence transformations, particularly around ROPE and SiLU. Specifically:

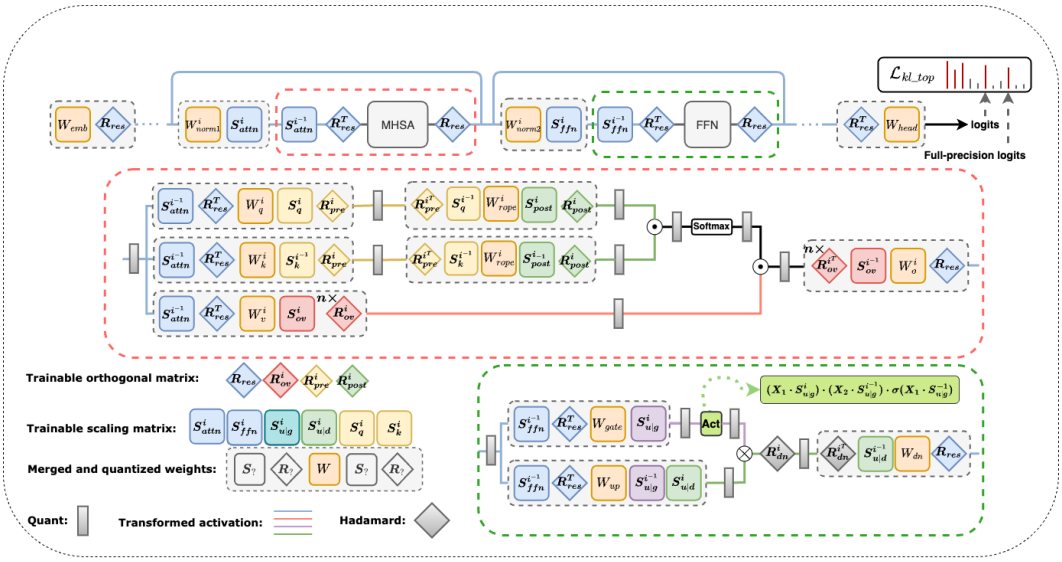

Figure 9: The extension of OSTQuant for full quantization.

1. **ROPE Handling**: We treat ROPE as a lightweight GEMM layer and construct a weight matrix of shape $(\text{token}, \text{head_dim}, \text{head_dim})$ based on its principle. We then introduce pre-ROPE and post-ROPE transformation pairs.
   a. Pre-ROPE transformations are based on the fact that ROPE and the preceding linear layer can be viewed as consecutive matrix multiplications along the head_dim. The corresponding transformation pairs are represented in figure by$\boldsymbol{S_q^i R_{pre}^i}$nd $\boldsymbol{S_k^i R_{pre}^i}$.
   b. Post-ROPE transformations rely on the attention computation formula $\boldsymbol{Attn} = \boldsymbol{Q@K}^\top$, where $\boldsymbol{Q}$ means the query matrix and $\boldsymbol{K}$ means the key matrix in Self-Attention module. The corresponding transformation pairs are represented in figure by $\boldsymbol{S_{post}^i R_{post}^i}$
2. **Smoothing Activation Discrepancies of SiLU**: Inspired by smoothing methods for SwiGLU in I-LLM (Hu et al., 2024), we decompose SiLU as $\text{SiLU}(\boldsymbol{X}) = \boldsymbol{X} \cdot \sigma(\boldsymbol{X})$ and use equivalences such as

$$\boldsymbol{X_1} \cdot \boldsymbol{X_2} \cdot \boldsymbol{\sigma}(\boldsymbol{X_1}) = (\boldsymbol{X_1} \cdot \boldsymbol{S}) \cdot (\boldsymbol{S_2} \cdot \frac{\boldsymbol{1}}{\boldsymbol{S}}) \cdot \boldsymbol{\sigma}((\boldsymbol{X_1} \cdot \boldsymbol{S}) \cdot \frac{\boldsymbol{1}}{\boldsymbol{S}})$$

   to alleviate inter-channel discrepancies of activations before and after SiLU. The corresponding transformation is represented in figure by $\boldsymbol{S_{u|g}}$.

We will conduct experiments in full-quantization domain in the future to fully explore the potential of OSTQuant.

A.6 Full Results

A.6.1 Quantitative results

In this section, we provide a comprehensive presentation of our results across various datasets to complement the main paper. Specifically, the results include:

- Complete comparison of the perplexity score on WikiText2 and averaged accuracy on zero-shot common sense reasoning tasks on LLaMA-1(Tab 13), 2 and 3 (Tab 12).
- Validate the effectiveness of OSTQuant on larger-scale language models such as LLaMA-2-70B and LLaMA-3-70B(Tab 14).

Table 12: Complete omparison of the perplexity score on WikiText2 and averaged accuracy on Zero-shot Common Sense Reasoning tasks on **LLaMA-2 & 3**.

Model	#Bits W-A-KV	Method	ARC-c (↑)	ARC-e (↑)	BoolQ (↑)	HellaS. (↑)	Lam. (↑)	OBQA (↑)	PIQA (↑)	SIQA (↑)	WinoG. (↑)	Avg. (↑)	Wiki2 (↓)
2-7B	16-16-16	Full Precision	46.42	74.33	77.71	75.94	73.69	44.20	79.16	45.91	69.53	65.21	5.47
	4-16-16	RTN	42.15	67.59	73.06	72.34	67.18	41.80	76.50	44.11	66.69	61.27	7.02
		SmoothQuant	39.59	65.19	69.82	68.84	62.27	40.20	75.95	44.17	63.85	58.88	8.03
		GPTQ	42.49	69.53	61.31	73.83	67.61	42.40	77.64	44.52	68.43	60.86	9.84
		Omniquant	42.49	71.00	74.34	73.85	70.70	44.20	78.40	44.93	68.82	63.19	5.74
		AWQ	44.11	70.75	78.07	74.98	70.68	43.80	78.13	45.14	69.38	63.89	5.83
		QuaRot	43.94	73.15	76.97	74.87	73.06	44.00	78.24	45.09	69.38	64.30	5.62
		SpinQuant	43.34	72.69	73.36	75.10	73.80	43.00	77.86	45.60	67.56	63.59	5.58
		OSTQuant	44.54	73.31	75.57	75.04	73.67	44.20	78.89	45.50	68.59	64.37	5.64
	4-4-16	RTN	25.34	28.03	50.52	27.71	1.01	26.20	50.82	33.93	48.38	32.44	nan
		SmoothQuant	28.33	26.39	49.39	27.28	1.18	23.40	48.80	33.62	50.75	32.13	nan
		GPTQ	24.40	28.70	51.62	28.66	1.36	24.60	51.14	34.49	49.49	32.72	nan
		QuaRot	42.32	69.65	74.77	72.91	70.81	39.80	77.20	43.55	65.82	61.87	6.05
		SpinQuant	37.54	62.58	71.16	70.48	67.16	34.80	75.46	39.76	60.62	57.37	6.78
		OSTQuant	44.03	71.93	75.41	74.94	73.22	43.20	78.51	45.85	68.03	63.90	5.60
	4-4-4	RTN	27.22	27.06	50.83	27.34	0.93	25.80	49.51	34.85	50.51	32.67	nan
		SmoothQuant	26.37	25.63	47.71	27.05	1.11	26.40	51.90	34.49	48.38	32.12	nan
		GPTQ	26.96	27.65	52.84	28.83	1.63	29.20	49.62	35.11	49.80	33.52	nan
		Omniquant	31.40	53.75	63.79	55.06	35.63	34.40	66.59	40.28	54.70	48.40	14.26
		QuaRot	41.43	69.32	74.19	72.50	70.66	39.80	77.42	43.35	64.64	61.48	6.11
		SpinQuant	40.44	71.08	74.40	73.51	70.66	41.80	76.88	43.50	65.82	62.01	5.96
		OSTQuant	42.92	72.56	74.71	73.14	71.76	44.40	77.42	44.98	66.77	63.18	5.91
2-13B	16-16-16	Full Precision	49.15	77.53	80.58	79.39	76.62	45.20	80.63	47.49	71.90	67.61	4.88
	4-16-16	RTN	42.92	66.54	71.38	66.62	68.99	39.40	76.93	44.06	65.35	60.24	6.39
		SmoothQuant	46.25	70.45	74.92	69.16	70.49	39.80	77.86	45.14	64.17	62.03	5.86
		GPTQ	49.63	73.95	74.83	73.77	73.20	42.40	78.51	45.50	70.64	64.71	5.79
		Omniquant	48.29	75.42	77.92	77.80	75.59	45.20	80.41	46.62	70.17	66.38	5.02
		AWQ	48.63	78.16	78.81	78.48	75.20	45.00	79.54	46.21	72.45	66.25	5.07
		QuaRot	49.15	76.26	80.46	78.17	76.50	45.40	80.03	45.50	71.11	66.95	5.00
		SpinQuant	49.15	77.48	79.27	78.46	77.10	44.60	80.03	46.47	71.67	67.14	5.00
		OSTQuant	48.72	76.26	80.67	78.27	76.54	45.54	80.25	47.65	71.90	67.31	4.94
	4-4-16	RTN	27.99	26.81	38.50	26.08	0.00	23.60	48.20	34.90	51.62	30.86	8e3
		SmoothQuant	24.49	35.06	47.98	30.87	3.67	26.20	55.01	35.31	49.72	34.26	1e3
		GPTQ	27.82	26.77	37.92	25.67	0.00	21.80	47.77	35.11	48.15	30.11	4e3
		QuaRot	46.42	73.86	78.10	75.68	74.31	43.00	79.05	44.37	71.35	65.13	5.35
		SpinQuant	43.77	69.99	76.57	74.63	72.81	41.60	77.20	44.27	68.19	63.23	5.24
		OSTQuant	47.78	74.66	80.03	77.60	75.94	44.40	79.38	46.06	70.32	66.24	5.14
	4-4-4	RTN	27.82	26.52	38.38	26.27	0.02	26.00	49.78	34.39	49.17	30.93	7e3
		SmoothQuant	24.49	33.00	45.84	30.70	2.70	23.80	53.81	34.80	51.07	33.36	2e3
		GPTQ	27.90	26.39	37.95	26.16	0.00	27.00	48.26	34.39	50.43	27.85	5e3
		Omniquant	32.85	55.13	64.34	60.13	42.85	33.40	68.17	39.76	56.51	50.35	12.30
		QuaRot	47.27	73.91	78.41	75.33	73.53	43.80	79.27	45.85	69.06	65.16	5.39
		SpinQuant	46.67	74.49	76.76	75.22	72.19	42.40	78.29	43.45	67.72	64.13	5.74
		OSTQuant	47.10	75.21	77.46	76.71	75.14	44.60	78.67	45.75	68.03	65.41	5.25
3-8B	16-16-16	Full Precision	53.50	77.74	81.10	79.18	75.74	44.80	80.63	47.08	73.01	68.09	6.14
	4-16-16	RTN	48.98	73.23	72.75	75.90	63.85	43.20	78.40	43.81	73.16	63.70	8.13
		SmoothQuant	47.44	72.35	72.11	74.92	62.41	43.00	77.69	43.91	71.27	62.79	8.12
		GPTQ	49.74	72.52	71.28	68.34	46.69	43.60	78.78	46.47	71.82	61.03	7.43
		Omniquant	50.09	74.54	79.51	76.92	70.31	43.80	79.54	44.52	71.74	65.66	7.19
		AWQ	52.22	76.68	80.31	77.51	74.81	44.20	79.60	46.26	71.67	67.03	7.36
		QuaRot	51.88	77.53	79.60	77.87	74.11	44.40	80.14	46.37	73.56	67.27	6.53
		SpinQuant	52.13	72.28	79.20	78.40	73.76	44.80	79.98	45.50	72.77	66.54	6.49
		OSTQuant	52.82	79.84	80.31	77.86	76.48	42.80	80.74	45.55	73.80	67.80	6.53
	4-4-16	RTN	23.72	30.89	46.30	31.26	3.03	27.60	52.72	35.26	50.04	33.42	6e2
		SmoothQuant	23.29	28.28	48.93	29.19	1.57	28.60	54.46	33.37	49.64	33.04	1e3
		GPTQ	23.46	32.07	43.79	30.10	2.41	28.00	53.97	34.14	48.86	32.98	6e2
		QuaRot	42.66	67.26	73.73	73.60	67.42	43.00	76.61	45.04	65.90	61.69	8.02
		SpinQuant	47.35	74.12	76.36	75.98	69.88	42.46	77.37	44.47	68.98	64.11	7.28
		OSTQuant	48.81	73.48	79.82	75.97	72.62	42.40	78.18	45.75	69.22	65.14	7.24
	4-4-4	RTN	23.72	30.56	46.18	29.83	2.70	28.60	52.45	34.39	50.20	33.18	7e2
		SmoothQuant	23.55	28.96	48.84	28.90	1.44	29.40	51.09	34.14	50.36	32.96	1e3
		GPTQ	23.38	32.74	44.34	29.72	2.39	29.80	54.95	34.75	51.30	33.71	6e2
		Omniquant	22.87	30.35	41.53	31.11	1.86	25.40	53.37	34.08	50.43	32.33	4e2
		QuaRot	42.83	67.42	73.21	72.66	66.93	42.20	75.73	45.19	66.22	61.38	8.18
		SpinQuant	46.33	73.57	76.15	75.43	71.40	41.40	79.16	44.68	68.75	64.10	7.35
		OSTQuant	49.32	76.73	78.87	76.01	70.77	43.20	78.51	45.70	69.22	65.37	7.29

Table 13: Complete omparison of the perplexity score on WikiText2 and averaged accuracy on Zero-shot Common Sense Reasoning tasks on **LLaMA**.

Model	#Bits W-A-KV	Method	ARC-c (↑)	ARC-e (↑)	BoolQ (↑)	HellaS. (↑)	LambA. (↑)	OBQA (↑)	PIQA (↑)	SIQA (↑)	WinoG. (↑)	Avg. (↑)	Wiki2 (↓)
7B	16-16-16	Full Precision	44.71	72.90	74.98	76.20	73.08	43.80	79.16	45.55	69.93	64.48	5.68
	4-16-16	RTN	43.17	69.82	73.30	73.75	69.67	42.00	78.13	45.34	68.82	62.67	7.94
		SmoothQuant	40.96	68.60	74.04	73.16	68.74	42.00	78.07	46.11	68.51	62.24	7.46
		GPTQ	41.72	67.85	67.98	69.50	63.15	40.80	76.55	44.37	69.46	60.15	7.93
		Omniquant	42.49	71.38	74.62	74.71	71.98	42.00	79.05	45.96	68.59	63.42	5.86
		AWQ	43.86	70.79	74.19	75.27	69.94	43.00	78.45	45.09	69.14	63.30	5.97
		QuaRot	42.75	69.99	73.30	75.13	73.55	42.80	78.35	45.14	69.61	63.40	5.83
		SpinQuant	43.77	71.17	74.46	75.09	72.91	44.40	78.40	44.52	70.72	63.94	5.76
		OSTQuant	44.20	72.56	73.73	75.05	73.45	44.60	78.73	45.45	69.38	64.13	5.81
	4-4-16	RTN	23.46	29.34	45.05	29.02	1.24	26.00	52.07	35.11	51.30	32.51	7e3
		SmoothQuant	25.17	31.40	51.62	29.73	5.43	28.20	54.68	34.44	49.09	34.42	3e2
		GPTQ	23.89	27.74	42.87	28.49	1.28	27.40	51.00	36.23	50.20	32.12	1e3
		QuaRot	40.36	67.26	73.15	72.89	70.81	42.00	77.97	44.27	67.17	61.76	6.22
		SpinQuant	40.19	68.43	72.35	72.91	70.68	41.20	77.75	44.17	68.67	61.82	6.08
		OSTQuant	42.58	70.79	72.87	74.06	70.77	43.40	77.69	45.04	67.25	62.72	6.04
	4-4-4	RTN	23.89	29.59	46.67	28.37	1.13	26.40	52.99	35.21	51.54	32.87	1e4
		SmoothQuant	23.38	30.18	50.03	29.67	4.89	24.60	51.74	34.75	50.67	33.32	3e2
		GPTQ	23.89	27.90	43.88	27.86	1.05	26.20	51.85	34.08	49.49	31.80	2e3
		Omniquant	31.40	54.84	61.80	56.98	38.29	31.80	66.59	39.30	55.17	48.46	11.26
		QuaRot	40.27	67.55	72.20	72.59	70.62	39.80	77.20	44.88	65.90	61.22	6.26
		SpinQuant	39.08	68.18	73.06	72.87	70.46	40.60	77.42	42.68	67.56	61.32	6.12
		OSTQuant	42.92	70.33	72.11	73.77	70.66	42.42	77.91	44.93	67.88	62.55	6.07
13B	16-16-16	Full Precision	47.87	74.49	77.86	79.10	76.03	44.40	80.30	46.72	73.24	66.67	5.09
	4-16-16	RTN	45.56	70.66	72.45	76.06	70.58	42.00	78.84	44.93	70.01	63.45	8.60
		SmoothQuant	43.86	71.21	71.62	74.19	69.34	40.00	77.80	45.45	70.72	62.69	18.75
		GPTQ	45.99	72.85	73.27	75.31	70.10	44.60	79.87	46.16	71.11	64.36	6.58
		Omniquant	47.01	73.86	77.22	77.95	75.59	45.00	79.87	46.88	72.61	66.22	5.21
		AWQ	47.53	73.86	75.60	59.03	78.34	43.40	79.87	45.85	71.67	65.58	5.28
		QuaRot	47.18	72.22	76.85	78.07	75.99	45.00	79.76	45.70	72.38	65.91	5.20
		SpinQuant	47.44	74.83	77.37	78.13	75.55	45.60	79.92	46.01	72.06	66.32	5.16
		OSTQuant	48.04	73.86	78.10	78.28	75.99	45.60	80.52	46.93	72.30	66.62	5.21
	4-4-16	RTN	25.85	26.26	42.05	26.70	0.17	28.00	50.33	34.60	50.67	31.63	2e4
		SmoothQuant	25.43	29.29	51.56	28.12	2.02	26.00	53.32	34.34	49.57	33.29	6e2
		GPTQ	24.66	27.78	40.80	25.83	0.70	24.20	51.31	36.65	51.70	31.51	3e3
		QuaRot	46.93	71.51	75.57	76.63	74.13	42.40	78.73	45.24	68.98	64.46	5.50
		SpinQuant	45.73	72.56	75.38	76.86	73.28	43.60	78.89	44.63	70.40	64.59	5.36
		OSTQuant	48.04	74.07	77.13	77.22	74.58	45.00	78.62	46.16	71.35	65.80	5.40
	4-4-4	RTN	26.28	27.27	42.35	25.85	0.19	26.60	49.95	34.19	49.25	31.33	3e4
		SmoothQuant	24.49	28.83	51.65	27.91	2.08	26.00	52.56	35.41	50.59	33.28	5e2
		GPTQ	23.63	27.31	39.85	26.17	0.56	26.00	51.96	35,82	49.57	30.63	3e3
		Omniquant	29.61	48.23	58.20	56.45	28.76	31.40	65.29	37.10	55.64	45.63	10.87
		QuaRot	46.50	71.55	75.08	76.43	73.47	45.00	78.78	44.37	70.09	64.59	5.53
		SpinQuant	45.99	70.71	76.51	77.16	73.63	45.60	79.00	45.65	70.32	64.95	5.39
		OSTQuant	45.90	75.25	76.94	77.21	74.23	43.40	79.43	45.91	70.56	65.43	5.40
30B	16-16-16	Full Precision	52.99	80.39	82.75	82.62	77.59	48.00	82.26	47.75	75.69	70.00	4.10
	4-16-16	RTN	49.74	73.99	77.89	79.07	72.21	44.20	79.00	45.70	73.88	65.69	6.13
		SmoothQuant	48.98	72.94	80.00	79.00	71.49	44.80	78.13	45.96	73.16	65.69	5.80
		GPTQ	50.85	75.97	80.31	79.31	74.13	45.00	78.94	45.24	72.77	66.95	5.26
		Omniquant	52.22	78.62	81.80	81.94	76.85	47.20	81.07	47.54	74.43	69.07	4.25
		AWQ	53.24	77.48	81.68	82.29	76.79	48.20	81.72	48.16	75.37	69.44	4.28
		QuaRot	53.58	78.62	82.11	82.10	77.62	48.00	81.72	47.75	76.09	69.73	4.27
		SpinQuant	52.90	78.49	82.02	82.21	78.28	48.20	81.01	48.41	75.06	69.62	4.21
		OSTQuant	53.07	79.12	83.09	82.04	78.58	48.60	81.18	48.06	74.82	69.84	4.19
	4-4-16	RTN	25.00	27.95	42.02	27.22	0.21	27.00	49.13	34.65	50.91	31.57	2e3
		SmoothQuant	23.63	30.68	54.86	31.91	3.80	28.20	54.13	34.49	50.04	34.64	1e3
		GPTQ	27.30	27.19	38.69	26.75	0.17	25.80	49.02	35.21	47.75	30.88	2e3
		QuaRot	51.79	76.39	80.76	80.90	77.08	45.80	80.58	45.60	74.35	68.14	4.57
		SpinQuant	50.06	77.06	81.38	80.62	76.79	46.00	80.14	46.37	74.27	68.08	4.53
		OSTQuant	51.37	78.11	82.48	79.51	75.99	45.40	81.18	47.80	74.82	68.52	4.43
	4-4-4	RTN	25.00	28.87	44.07	27.29	0.39	25.60	49.67	34.54	49.33	31.64	2e3
		SmoothQuant	22.61	32.87	55.05	31.28	3.40	28.00	53.75	34.65	50.28	34.65	1e3
		GPTQ	27.22	27.82	39.36	27.13	0.33	24.80	50.71	34.34	47.91	31.07	2e3
		Omniquant	29.10	53.79	54.95	52.44	26.45	30.60	65.56	38.54	53.91	45.04	10.33
		QuaRot	51.71	76.98	80.95	80.86	77.04	46.20	80.63	45.00	73.32	68.08	4.60
		SpinQuant	51.62	76.98	81.07	80.57	76.63	46.00	79.92	46.26	74.19	68.14	4.55
		OSTQuant	49.74	76.52	81.16	81.13	77.57	46.40	80.90	46.11	74.27	68.20	4.42

Table 14: Complete comparison of the perplexity score on WikiText2 and averaged accuracy on Zero-shot Common Sense Reasoning tasks for **LLaMA2-70B and LLaMA3-70B**.

Model	#Bits W-A-KV	Method	ARC-c (↑)	ARC-e (↑)	BoolQ (↑)	HellaS. (↑)	LambA. (↑)	OBQA (↑)	PIQA (↑)	SIQA (↑)	WinoG. (↑)	Avg. (↑)	Wiki2 (↓)
2-70B	16-16-16	Full Precision	57.42	81.02	83.79	83.81	79.60	48.80	82.70	49.18	77.98	71.59	3.32
	4-16-16	RTN	55.80	79.29	81.35	81.78	75.51	47.60	81.94	46.83	76.48	69.62	3.87
		SmoothQuant	50.26	76.56	81.53	67.81	73.63	44.40	81.34	44.17	73.64	65.93	5.50
		GPTQ	56.91	80.81	83.24	82.47	79.06	47.80	82.75	48.06	77.51	70.96	3.94
		Omniquant	57.08	80.81	82.69	83.07	79.18	47.40	83.08	48.87	77.19	71.04	3.47
		AWQ	56.67	80.54	82.98	82.54	78.83	47.67	82.97	48.12	77.62	70.88	4.03
		QuaRot	57.34	80.85	83.24	83.27	80.38	47.60	82.21	48.62	77.35	71.21	3.41
		SpinQuant	56.91	80.60	83.18	83.06	79.16	49.00	82.75	48.31	77.11	71.12	3.43
		OSTQuant	57.36	81.37	83.20	83.86	79.77	48.73	82.69	48.46	77.89	71.48	3.41
	4-4-16	RTN	29.35	26.05	37.74	25.97	0.02	24.80	51.31	34.14	48.70	30.90	7e4
		SmoothQuant	25.00	35.98	55.23	32.52	7.49	25.00	54.62	35.21	51.70	35.86	3e2
		GPTQ	27.82	25.80	37.95	25.82	0.00	27.00	49.67	33.98	49.72	30.86	nan
		QuaRot	55.29	80.35	81.10	81.87	79.06	45.80	82.05	47.90	76.24	69.96	3.78
		SpinQuant	55.38	78.96	83.36	82.54	79.00	47.80	82.10	48.67	77.43	70.58	3.68
		OSTQuant	56.61	80.51	83.03	82.68	79.11	47.86	83.00	48.76	76.70	70.92	3.57
	4-4-4	RTN	30.38	27.74	38.23	26.12	0.02	24.60	51.74	34.29	52.49	31.73	7e4
		SmoothQuant	24.15	33.88	55.32	31.75	7.14	26.40	54.95	34.14	52.17	35.54	3e2
		GPTQ	28.75	26.39	37.86	25.96	0.00	26.40	50.00	34.44	50.04	31.09	nan
		QuaRot	56.48	80.56	81.59	81.93	79.16	46.00	82.21	48.00	76.80	70.30	3.80
		SpinQuant	56.31	80.64	83.55	82.36	79.41	47.20	82.21	47.29	76.16	70.57	3.61
		OSTQuant	56.58	80.17	83.64	82.49	78.72	48.00	82.76	48.67	76.49	70.84	3.59
3-70B	16-16-16	Full Precision	64.42	85.98	85.14	84.95	79.47	48.46	84.39	50.82	80.66	73.81	2.86
	4-16-16	RTN	26.28	25.55	37.83	26.36	0.00	29.00	50.98	34.70	49.64	31.15	1e4
		SmoothQuant	51.88	77.53	80.09	80.47	73.16	46.60	80.58	45.29	75.85	67.94	6.70
		GPTQ	25.77	25.29	37.83	26.36	0.12	28.40	51.74	34.90	52.64	31.45	9e3
		Omniquant	48.29	75.42	77.92	77.80	75.59	45.20	80.41	46.62	70.17	66.38	5.02
		AWQ	52.26	78.95	83.24	81.52	73.05	47.67	81.25	44.43	77.98	68.93	5.92
		QuaRot	62.20	83.88	85.57	84.18	79.04	48.20	83.13	50.10	80.03	72.93	3.53
		SpinQuant	62.03	84.97	85.11	84.06	78.30	47.00	83.90	49.85	80.90	72.90	3.49
		OSTQuant	63.76	85.82	84.99	85.16	79.53	48.45	84.26	51.01	80.22	73.69	3.19
	4-4-16	RTN	27.47	25.88	37.83	26.26	0.00	27.20	51.63	35.26	49.33	31.21	9e3
		SmoothQuant	25.60	34.47	50.46	32.48	1.98	30.00	54.24	33.83	48.93	34.67	2e2
		GPTQ	25.77	26.09	43.64	26.42	0.00	27.40	52.01	32.55	49.33	31.47	4e4
		QuaRot	50.60	73.65	77.46	77.83	71.96	43.20	78.13	45.29	71.90	65.56	6.35
		SpinQuant	53.84	77.69	80.24	78.19	73.06	45.00	78.67	43.24	73.01	66.99	6.10
		OSTQuant	61.84	84.56	84.14	82.47	77.08	46.07	83.38	50.23	80.13	72.21	3.97
	4-4-4	RTN	27.13	25.42	37.83	26.12	0.00	26.60	50.76	35.16	48.38	30.82	9e3
		SmoothQuant	23.46	31.48	48.81	29.22	4.13	28.00	52.56	34.95	51.22	33.76	3e2
		GPTQ	26.11	25.17	45.17	26.07	0.00	26.40	48.86	33.88	49.17	31.20	4e4
		QuaRot	49.49	74.37	79.16	77.22	71.69	42.29	78.89	43.87	71.03	65.33	6.60
		SpinQuant	51.88	76.39	80.98	76.50	71.43	43.46	79.27	44.17	72.69	66.31	6.24
		OSTQuant	61.29	82.39	83.43	83.25	75.90	48.93	81.73	51.24	77.01	71.69	4.01

A.6.2 VISUALIZATION RESULTS

- Fig 10 illustrates the trends of activation QSUR and evaluation loss during the training process of the LLaMA3-8B model.
- Fig 11 and Fig 12 shows the activation distribution of different layers in LLaMA-2-7B and LLaMA-3-8B.
- Fig 13 shows the impact of Weight Outlier Minimization Initialization (WOMI) on weight distribution and quantization error of different layers in LLaMA-2-7B.
- Fig 14 presents visual comparisons of the activation distributions and quantization errors for QuaRot, SpinQuant, and OSTQuant on selected layers of LLaMA-2-7B.

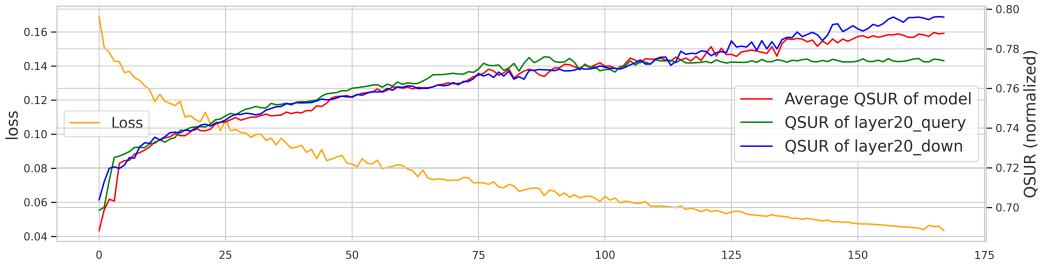

Figure 10: As the number of training iterations increases, the changes in the local and average QSURs, as well as the evaluation loss.

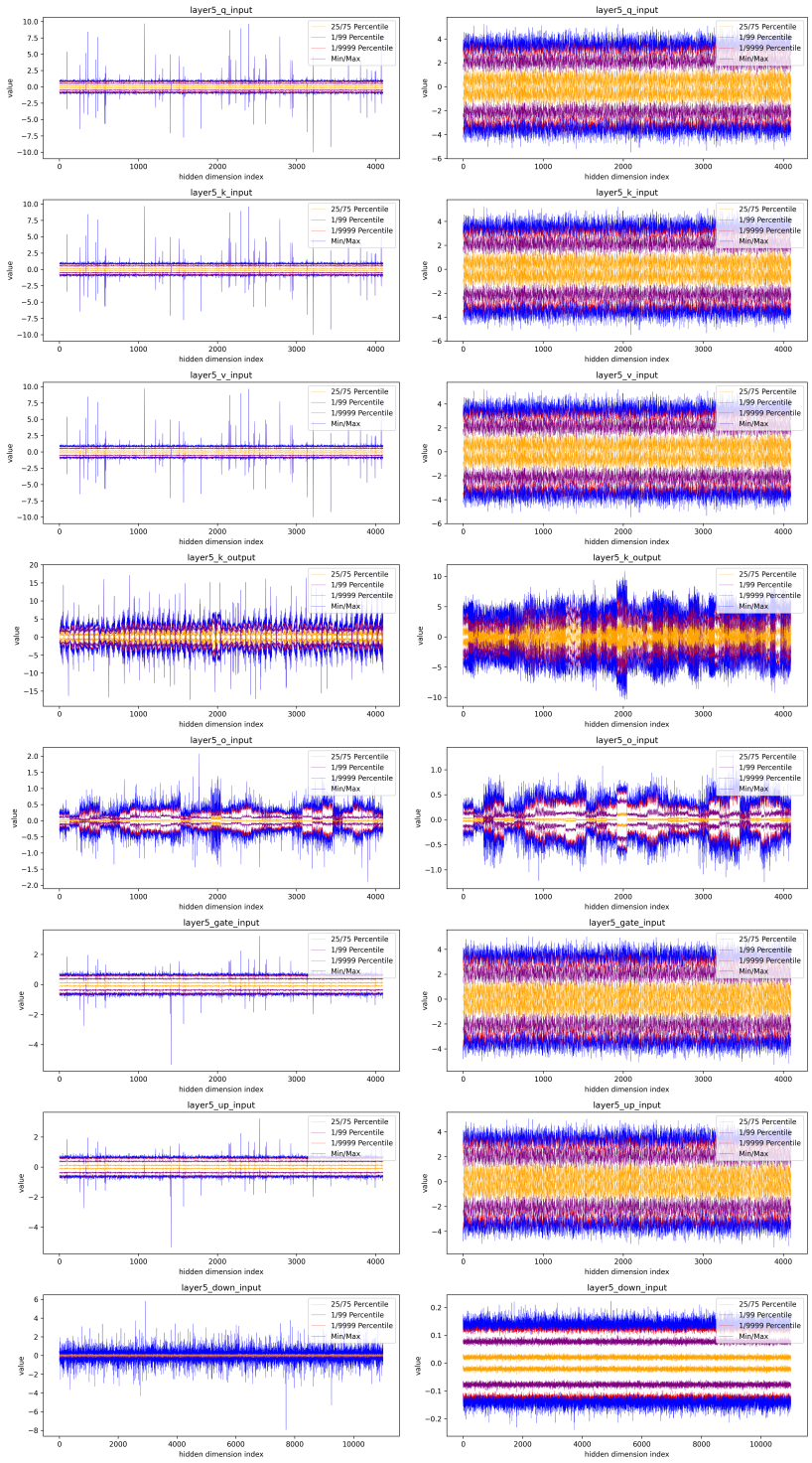

Figure 11: The activation distribution of different layers in LLaMA-2-7B before and after OSTQuant.

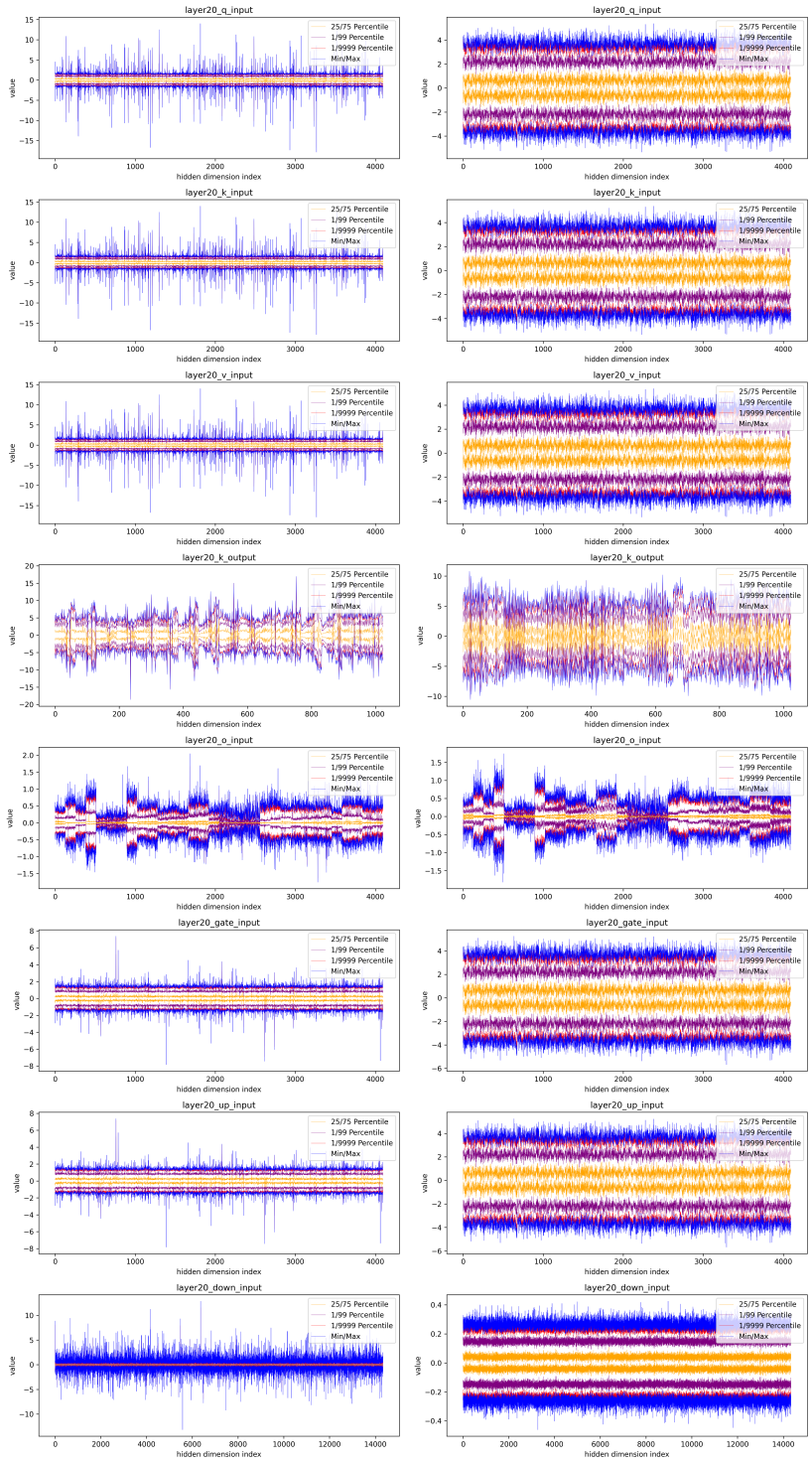

Figure 12: The activation distribution of different layers in LLaMA-3-8B before and after OSTQuant.

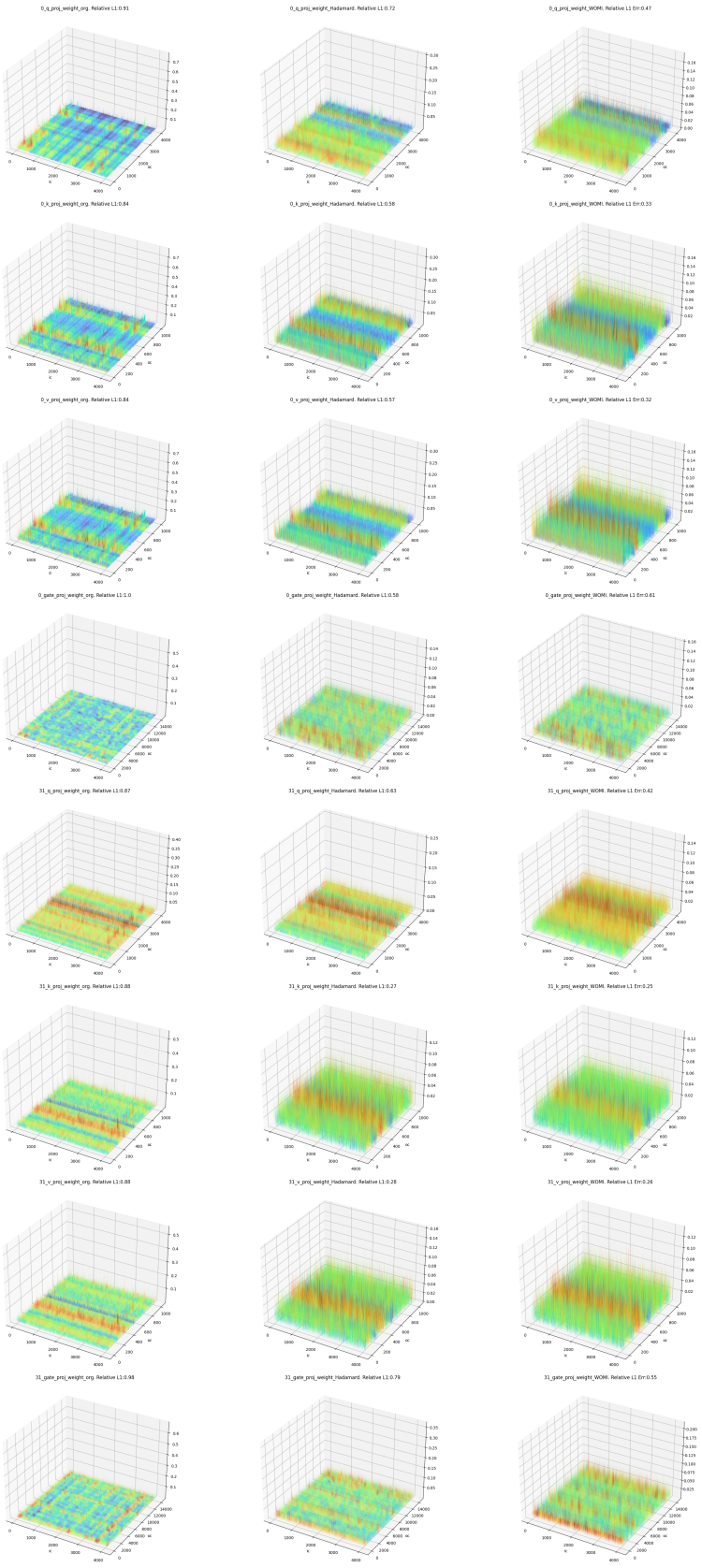

Figure 13: Visualizations comparing of the weight distribution and relative L1 error of LLaMA- 2-7B quantized with Ori (1st column), Hadamard transformed(2nd column), and WOMI transformed (3rd column), respectively.

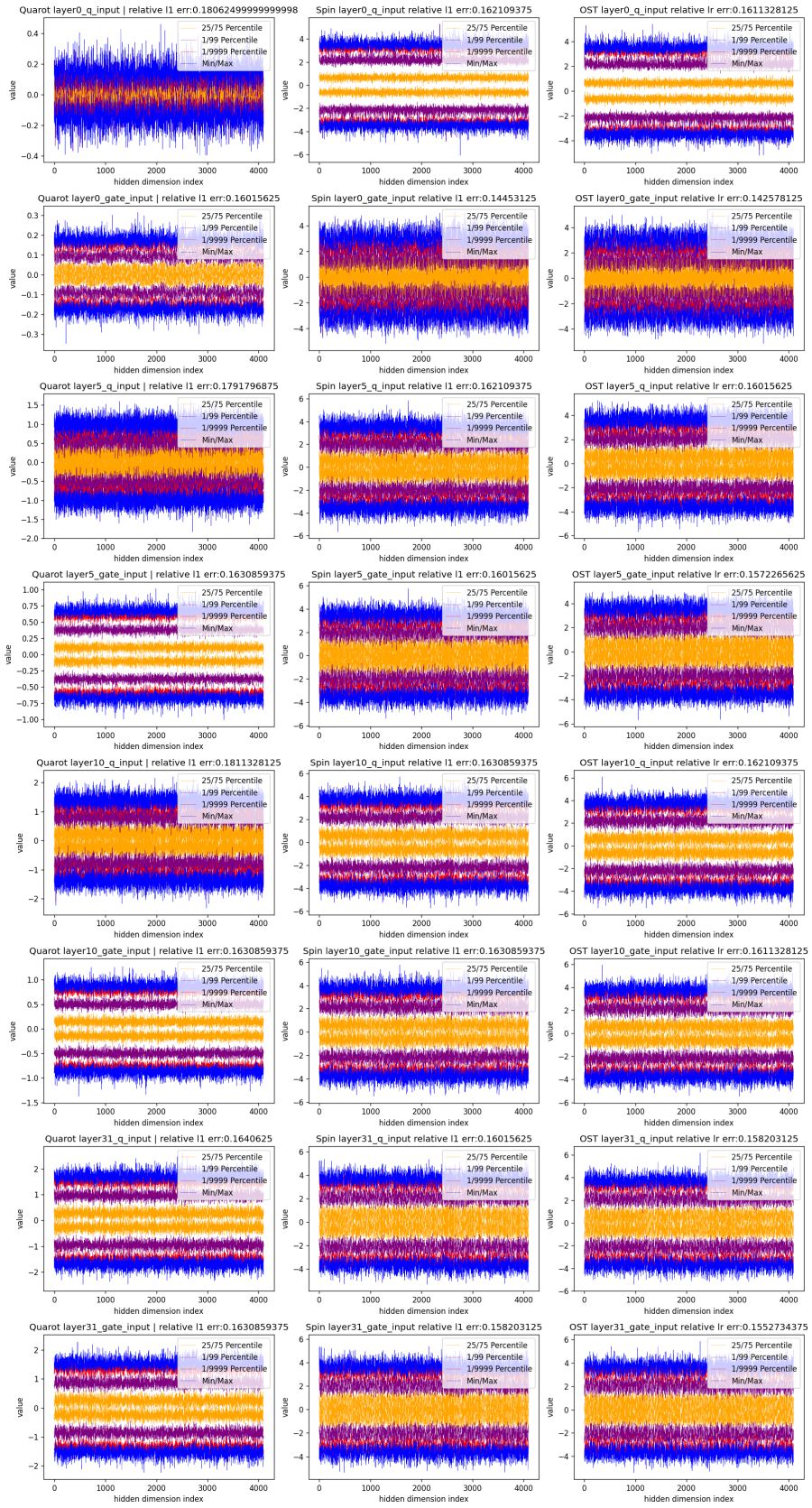

Figure 14: Visualizations comparing of the activation distribution and relative L1 error of LLaMA-2-7B quantized with QuaRot (1st column), SpinQuant (2nd column), and OSTQuant (3rd column), respectively. The relative L1 error here represents the difference between the activations before and after per-token quantization.